Delft University of Technology

Wind Turbine Stall-Induced Aeroelastic Instability Mitigation Using Vortex Generators

Meng, Qingshen; Chen, Chao; Hua, Xugang; Yu, Wei

Important note
To cite this publication, please use the final published version (if applicable).
Please check the document version above.

RESEARCH ARTICLE OPEN ACCESS

Wind Turbine Stall-Induced Aeroelastic Instability Mitigation Using Vortex Generators

Qingshen Meng[1,2] | Chao Chen[2] 🔟 | Xugang Hua[2] | Wei Yu[1] 🔟

[1]Wind Energy Section, Flow Physics and Technology, Faculty of Aerospace Engineering, Delft University of Technology, Delft, The Netherlands | [2]State Key Laboratory of Bridge Safety and Resilience, Hunan University, Changsha, China

Correspondence: Wei Yu (W.Yu@tudelft.nl) | Chao Chen (steinchen@hnu.edu.cn)

ABSTRACT

Inspired by Vortex Generators' success in delaying airfoil stall, this study explores the potential of using Vortex Generators to mitigate stall-induced instability in floating offshore wind turbines at parked and skewed inflow conditions for the first time. Significant improvements are achieved by strategically installing Vortex Generators in the outboard sections of turbine blades and optimizing their parameters (normalized height, length, inflow angle, and chordwise positions) using the particle swarm optimization algorithm and fast optimization method. Numerical results, including both linear and nonlinear stall instability analyses, consistently demonstrate that Vortex Generator arrays effectively mitigate stall-induced instability in the edgewise motion of wind turbines. The yaw misalignment angle range corresponding to the occurrence of edgewise instability is reduced by 29.69% (for NREL 5 MW wind turbine) and 22.95% (for IEA 15 MW wind turbine) while also decreasing limit cycle oscillation amplitudes. Additionally, azimuth angle does not influence optimization results, and implementing Vortex Generators can increase the onset wind speed of stall-induced instability without negatively affecting operating conditions.

1 | Introduction

With the increasing recognition of the vast potential of wind energy resources, the evolution of wind farms has led them to explore new possibilities, particularly in offshore locations and, even more specifically, deep-sea areas [1, 2]. Offshore wind farms have gained prominence due to several convincing advantages. One of the foremost benefits is the availability of a more consistent and robust wind resource, setting them apart from onshore ones. However, this transition to offshore wind farms, particularly in deep-sea locations, also brings unique challenges and considerations. One such challenge is the higher risk of stall-induced instability (or stall-induced vibration) [3–5]

on floating offshore wind turbines (FOWT). Stall-induced instability can occur when significant sections of a wind turbine blade experience moderate stall, typically defined here as an angle of attack (AoA) exceeding 15° but less than 40° [6, 7]. This condition generates extreme internal loads, as well as negative aerodynamic damping in the blade sections due to the negative lift-to-AoA gradient ($\partial C_L/\partial\alpha < 0$) [7]. While modern large-scale pitch-regulated turbines are designed to avoid stall conditions, unlike their stall-regulated predecessors. Studies indicate that stall-induced instability can still occur and induce severe edgewise vibrations [8], particularly during standstill scenarios, such as during installation, maintenance, or extreme wind events (such as typhoons) [9]. Under normal operating conditions,

the AoA for the inboard sections is more likely to exceed the static stall angle, potentially leading to stall in those sections. However, its contribution to the overall modal damping is quite limited and does not induce significant negative damping. When the wind turbine is in cut-out regions (standstill condition) and yaw misalignment occurs, the risk of blade stall becomes more pronounced [10]. Airfoil stall in outboard sections contributes more to the negative modal aerodynamic damping, making a wind turbine face a high risk of stall-induced instability. Stall-induced instability not only results in extreme loading but also contributes to fatigue loading on the blades, ultimately reducing their lifespan [7]. Therefore, it is important to evaluate the stall-induced instability of FOWTs with yaw misalignment during parked conditions and to develop engineering solutions and operational strategies to ensure the reliability and longevity of offshore wind farms.

Stall-induced instability has been a well-explored topic in wind turbine research, with considerable studies investigating this phenomenon across a range of onshore and offshore turbines. For instance, Risø National Laboratory coordinates a European project STABCON [11], which aims to develop reliable design tools for analyzing and optimizing large wind turbines concerning aeroelastic stability and active control. This project eventually gives several valuable deliverables, including the well-known aeroelastic stability tool for wind turbines, HAWCStab [12]. Hansen et al. [13, 14] provided a comprehensive framework for analyzing stall-induced instability in fixed wind turbines, with their analyses, as detailed in reference [13], and Chaviaropoulos' work [15], being rooted in linear structural dynamics. They use the damping ratio as the crucial criterion for assessing the stability of a specific mode, typically determined by calculating state-space eigenvalues. Furthermore, the assessment of stall-induced instability often involves examining overall damping ratios, as it is widely recognized that this instability arises due to negative damping, especially prevalent in wind turbines operating within the cut-out region. When addressing operational wind turbines, a practical approach involves converting system matrices into the Coleman domain [16, 17] using multi-blade coordinate transformation. In practice, wind turbines equipped with active pitch controllers during operation rarely experience stall-induced instability. In contrast, parked wind turbines in the cut-out region are at a higher risk of encountering this phenomenon [10]. Wang et al. [18] investigate the aeroelastic instability of an idling DTU 10 MW wind turbine, revealing that stall-induced instability cannot be thoroughly predicted through independent eigenvalue analysis. This paper also emphasizes that the out-of-plane modes exhibit the lowest damping ratio at a yaw misalignment of 30°, and the asymmetric out-of-plane tilt mode attains negative damping throughout the entire range of azimuth angles.

In the stability analysis of FOWTs, an essential step is developing a linear dynamic system to capture their dynamics. In this context, a central focus of our research is the acquisition of linear damping matrices arising from the interaction of inflow wind and wave propagation. This crucial aspect serves as the key point of our investigation. Traditionally, the determination of damping from inflow wind has been a classic issue within the field of aeroelasticity. In the work of Hansen [19], he introduced the concept of aerodynamic damping, emphasizing its pivotal

role in accurately predicting wind turbine instability. Petersen et al. [4] expanded on this notion, deriving explicit aerodynamic damping matrices tailored for stall-regulated wind turbines. They demonstrated a strong correlation between aerodynamic damping and the characteristics of airfoil lift and drag coefficient curves, as well as the rotational angular speed of the turbine. Further advancing the understanding of aerodynamic damping, Thomsen et al. [20] introduced an experimental method for determining edgewise-direction aerodynamic damping. They successfully implemented this method on the Bonus wind turbine, shedding light on an essential aspect of stability analysis. Chen et al. [21] developed a wavelet-based linearization method that enables the evaluation of aerodynamic damping for operating wind turbines. The FAST code also enters this field, offering a numerical strategy for obtaining aerodynamic damping through central difference equations [22, 23]. It facilitates the determination of damping matrices across various operating positions. Besides, HAWC2 [24] also includes a linearized aerodynamics module that enables aerodynamic damping analysis. While much has been accomplished regarding the aerodynamic damping of FOWT, the field of hydrodynamic damping through analytical means has remained relatively unexplored. Li et al. [25] proposed an approach based on potential flow theory for identifying damping arising from waves. Similarly, Meng et al. [26] dedicate the evaluation of viscous damping from wave-induced forces by linearizing Morison's equation.

Although much literature has focused on instability assessments, its investigation into mitigation measures is still insufficient. The core of stability enhancement is improving the damping of specific modes. Widely recognized methods can be classified as passive or active manners. A representative example is the DAMPBLADE project [27] for the former, while active trailing-edge flaps [28] could be an example for the latter. Moreover, the DAMPBLADE project and trailing-edge flaps adopted aeroelastic approaches. Structural damping augment approaches have been widely investigated through considerable research. For example, Li et al. [29] proposed a unidirectional cable pendulum damper to mitigate the large-scale wind turbine blade's vibration in an edgewise direction. Basu et al. [30] strengthened the damping in the edgewise direction by employing circular liquid dampers. In contrast, aerodynamic damping enhancement devices have not yet drawn enough attention, and although Hansen [19] pointed out that increasing the slope of the lift coefficient curve helps lift aerodynamic damping for a specific airfoil section, a detailed lift coefficient polar enhancement device has not been studied in depth.

Vortex Generators, often abbreviated as VGs, are increasingly finding applications in diverse industries ranging from aerospace to renewable energy, especially in the context of wind turbines. The implementation of VGs in wind turbines involves the strategic placement of small, winglet-like devices on the surfaces of airfoils or structures for inboard sections, and their effects have been confirmed through both numerical [31, 32] and experimental approaches [32]. By carefully configuring the size, spacing, and orientation of these VGs, engineers can adjust their effects to specific objectives. One crucial aspect of VG implementation in wind turbines is their ability to delay flow separation [33]. As wind passes through a turbine blade, it follows the contour of the airfoil shape, and as it moves towards

the trailing edge, there is a risk of boundary layer separation. This separation can lead to a decrease in lift and an increase in drag, ultimately impacting the turbine's performance. However, VGs strategically positioned along the blade can mitigate this issue by energizing the boundary layer and delaying separation, thus maintaining lift and reducing drag and eventually enhancing annual electricity production(AEP) [32, 34–36]. This paper intends to advocate VGs as one device to boost aerodynamic damping and stability performance. Although a great number of studies have taken place to widen the role of VGs in delaying stall of wind turbine blade inboard sections [37, 38], they remain undeveloped in attempting to promote the performance of stall-induced instability within rotor class.

The aerodynamic performance of VG-equipped airfoils can be evaluated through several approaches, among which the most convincing is the wind tunnel experiment [39]. However, due to the high cost of the direct wind tunnel experiment, the Navier-Stokes-based CFD tools can always be adopted as an alternative, and the CFD-based VG simulation method has been developed in the past several years. For example, Sørensen et al. [40] propose a method to predict the airfoil performance equipped with VGs, and decent agreement between the developed method and measurements from the Stuttgart Laminar Wind Tunnel [39] has been achieved in their study. The CFD technique is computationally expensive, especially when conducting optimizations for VG arrangements. Thus, a more efficient engineering model should be developed. Tavernier et al. [41] extended XFoil to analyze the effect of VGs on airfoil performance in a time-efficient way, the new version was named XFoilVG. The developed tool can empirically account for the effect of the VG height, length, inflow angle, and chordwise position on the airfoil's aerodynamic properties. The vortex-based method is computationally cheap and efficient for use in optimizations.

This paper is organized as follows: Section 2 introduces linearized aerodynamic and hydrodynamic damping matrices, provides a damping ratio calculation method, and introduces the particle swarm optimization (PSO) method that will be adopted for further VGs optimization. Section 3 is designed to provide some fundamental results for instability analyses. Section 4 presents the optimization results of VG configuration to reduce the risk of stall-induced instability, another fast optimization (FO) method is also introduced to speed up the optimization. Section 5 discusses the effects of azimuthal position, wind speeds, and different operational conditions when carrying out the optimizations, and the effect of VGs on tower and platform movements is also studied. Section 6 concludes the paper.

2 | Methodology

This section aims to introduce a linearized approach for calculating aerodynamic loads. Furthermore, we will introduce hydrodynamics, containing both viscous and radiation effects, and linear mooring line and hydrostatic stiffness in our model, which has already been discussed in detail in our previous publications [26]. Finally, we will present an algorithm to optimize stability enhancement using VGs in our wind turbine stability analysis.

2.1 | Model Description

This research is mainly based on the OC3 5 MW wind turbine, a benchmark model proposed by NREL as documented in publications [42, 43]. Besides, an IEA 15 MW wind turbine [44] is also being considered for performance optimization to confirm the effectiveness of VGs on different rotors. To enhance the accuracy of simulating the FOWT, this section employs a customized finite element (FE) model introduced by the authors' recent research [45].

A comprehensive horizontal axis FOWT is composed of several critical components, including a rotor with three blades, a central hub, a nacelle housing the generator and other essential machinery, a towering support structure, a floating platform, and a mooring line system designed to constraint the floater's mobility. This intricate assembly is thoroughly documented in prior research [43], and its schematic representation can be found in Figure 1. For a deeper understanding of FOWT and its dynamic behavior, it is crucial to consider the modes associated with these components, detailed in earlier studies [46]. These encompass the platform's translational modes, namely surge, sway, and heave, as well as its rotational modes, including pitch, roll, and yaw. Additionally, the tower exhibits Side-Side (SS) and Fore-Aft (FA) modes, while the blades possess flapwise and edgewise modes. These modes collectively characterize the complex dynamics of the FOWT system and are crucial in its analysis and modeling.
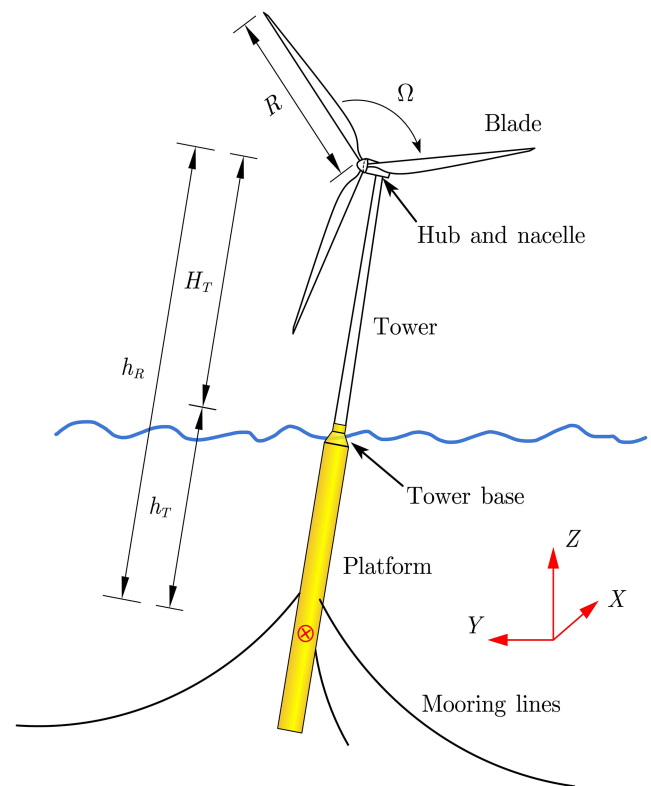
FIGURE 1 | NREL OC3 5 MW floating wind turbine structural layout.

2.2 | Aerodynamic Damping for a Standstill FOWT

This study adopts the quasi-steady blade element model to derive the aerodynamics damping. The airfoils' quasi-steady aerodynamic loads (lift dL and drag dD) can then be determined from the aerodynamic lift and drag coefficients (C_l and C_d) definition equations [47]:

$$
\begin{aligned}
dL(r, \alpha) &= \frac{1}{2} \rho_a c(r) V_{\text{rel}}^2(r) C_l(r, \alpha) \\
dD(r, \alpha) &= \frac{1}{2} \rho_a c(r) V_{\text{rel}}^2(r) C_d(r, \alpha)
\end{aligned}
\tag{1}
$$

in which ρ_a is the air density, c is the chord length, r is the radial position of an airfoil section, and the wind velocity V_{rel} is the overall real wind speed that the airfoil perceives in the $y_b - z_b$ plane:
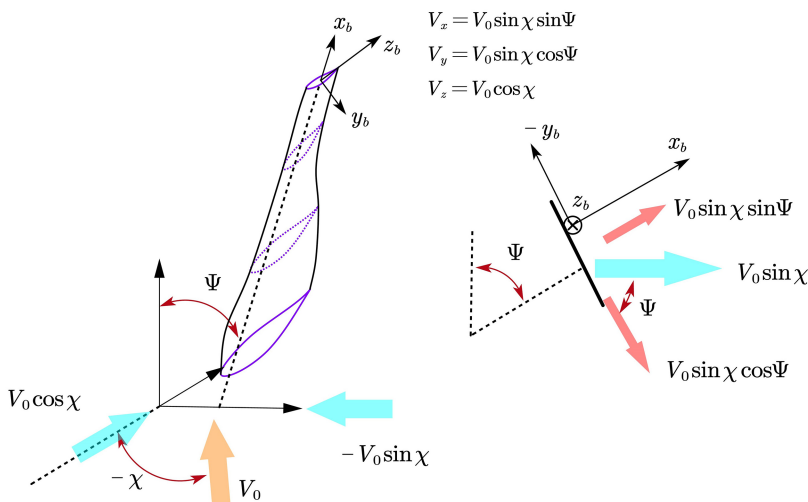
$$
V_{\text{rel}}^2 = V_{By,i,j}^2 + V_{Bz,i,j}^2
\tag{2}
$$

where the $V_{By,i,j}$ and $V_{Bz,i,j}$ represent the perceived wind speed along y_b and z_b directions considering the coupling effect with FOWT vibrations respectively, their accurate expressions can be derived as:

$$
\begin{aligned}
V_{By,i,j} &= V_y - x_b\left(\dot{U}_4 + \dot{u}_{\theta_y}^{\text{top}}\right) - \dot{v}_{y,i,j} \sin\beta + \dot{v}_{z,i,j} \cos\beta \\
&\quad + \left(\dot{U}_2 - h_R \dot{U}_4 + \dot{u}_z^{\text{top}}\right) \cos\Psi_j(t) \\
&\quad + \left(\dot{U}_3 + \dot{u}_x^{\text{top}}\right) \sin\Psi_j(t) \\
V_{Bz,i,j} &= V_z - \left(\dot{U}_1 + h_R \dot{U}_5 + \dot{u}_y^{\text{top}}\right) - \dot{v}_{y,i,j} \cos\beta - \dot{v}_{z,i,j} \sin\beta \\
&\quad - x_b\left(\dot{U}_5 + \dot{u}_{\theta_z}^{\text{top}}\right) \cos\Psi_j(t) \\
&\quad - x_b\left(\dot{U}_6 + \dot{u}_{\theta_x}^{\text{top}}\right) \sin\Psi_j(t)
\end{aligned}
\tag{3}
$$

in which, V_y and V_z can be given according to Figure 2 as:

$$
\begin{aligned}
V_y &= V_0 \sin\chi \cos\Psi = V_0' \sin\chi' \\
V_z &= V_0 \cos\chi = V_0' \cos\chi' \\
V_0' &= \sqrt{V_y^2 + V_z^2}
\end{aligned}
\tag{4}
$$

in which, χ' is defined as the effective yaw misalignment angle, accounting for the effect of azimuth angle:

$$
\chi' = \arctan \frac{V_y}{V_z}
\tag{5}
$$

Besides, x_b represents the location of an airfoil section along the blade lengthwise direction: $x_b = r$. β is the pitch angle, and $\beta = 90°$ when the blade is feathered under the parked condition. h_R is defined in Figure 1, and Ψ_j indicates the azimuth angle of the jth blade. Furthermore, several velocities for FOWT components included in Equation (3) can be assembled in blade($\mathbf{v}^e$), tower($\mathbf{u}^{\text{top,e}}$) and platform($\mathbf{U}$) degrees of freedom (DOFs) vectors:

$$
\begin{aligned}
\dot{\mathbf{U}} &= \left\{\dot{U}_1, \dot{U}_2, \dot{U}_3, \dot{U}_4, \dot{U}_5, \dot{U}_6\right\}^T \\
\dot{\mathbf{u}}^{\text{top,e}} &= \left\{\dot{u}_x^{\text{top}}, \dot{u}_y^{\text{top}}, \dot{u}_z^{\text{top}}, \dot{u}_{\theta_x}^{\text{top}}, \dot{u}_{\theta_y}^{\text{top}}, \dot{u}_{\theta_z}^{\text{top}}\right\}^T \\
\dot{\mathbf{v}}^e &= \left\{\dot{v}_{x,i,j}, \dot{v}_{y,i,j}, \dot{v}_{z,i,j}, \dot{v}_{\theta_x,i,j}, \dot{v}_{\theta_y,i,j}, \dot{v}_{\theta_z,i,j}\right\}^T
\end{aligned}
\tag{6}
$$

Additionally, lift and drag coefficients in Equation (1) are functions versus local AoA α of an airfoil. When considering azimuth angle, the AoA is defined in Figure 2, with the relation:

$$
\hat{\chi} = \chi' + \frac{\pi}{2} = \alpha + \theta_t + \beta
\tag{7}
$$

in which θ_t represents the twist angle. Thus,

$$
\alpha = \chi' - \left(\theta_t + \beta - \frac{\pi}{2}\right)
\tag{8}
$$

Specifically, $\chi' = \chi$ when the yaw misalignment angle is 0. Their geometric relationship is provided in Figure 2.

Aerodynamic loads are expected to be projected in the rotor plane as follows:

$$
\begin{aligned}
dT &= dL \cos\chi + dD \sin\chi \\
dS &= -dL \sin\chi + dD \cos\chi
\end{aligned}
\tag{9}
$$

FIGURE 2 | Local angle of attack definition for a standstill wind turbine airfoil.
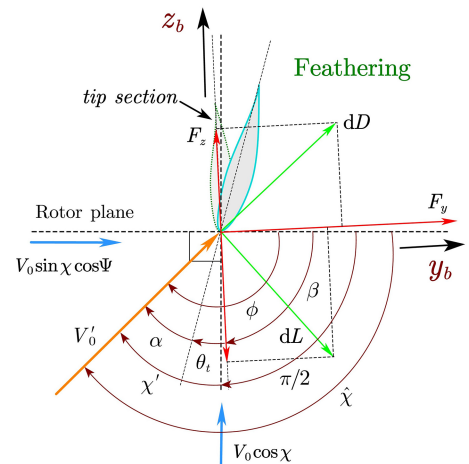
Aerodynamic force vector $\mathbf{F}_{\text{Aero}}$ in CS $x_b - y_b - z_b$ can be written after obtaining dT and dS by considering pitch angle β, and can be further expressed through FOWT velocity vectors as:

$$\mathbf{F}_{\text{Aero}} = \mathbf{F}_{\text{Aero}}\left(\dot{\mathbf{v}}^e, \dot{\mathbf{u}}^{\text{top,e}}, \dot{\mathbf{U}}\right) \tag{10}$$

According to the previous study [4], aerodynamic loads on blade sections have the following form, by assuming blade, tower and platform velocities small quantities:

$$\mathbf{F}_{\text{Aerob}}^* = \mathbf{F}_{\text{Aerob}}^{0*} - \begin{bmatrix} \mathbf{C}_{\text{Aerobb}}^* & \mathbf{C}_{\text{Aerobt}}^* & \mathbf{C}_{\text{Aerobp}}^* \end{bmatrix} \begin{Bmatrix} \dot{\mathbf{v}}^e \\ \dot{\mathbf{u}}^{\text{top,e}} \\ \dot{\mathbf{U}} \end{Bmatrix} \tag{11}$$

with,

$$\mathbf{C}_{\text{Aerobb}}^* = \frac{\partial \mathbf{F}_{\text{Aerob}}^*}{\partial \dot{\mathbf{v}}^e}, \ \mathbf{C}_{\text{Aerobt}}^* = \frac{\partial \mathbf{F}_{\text{Aerob}}^*}{\partial \dot{\mathbf{u}}^{\text{top,e}}}, \ \mathbf{C}_{\text{Aerobp}}^* = \frac{\partial \mathbf{F}_{\text{Aerob}}^*}{\partial \dot{\mathbf{U}}} \tag{12}$$

Here, $\mathbf{F}_{\text{Aerob}}^*$ represents the aerodynamic load vector acting on blade nodes. This load vector can be described as a combination of a steady static aerodynamic load vector $\mathbf{F}_{\text{Aerob}}^{0*}$ and the contributions from aerodynamic damping loads. Specifically, an example of edgewise-corresponding $c_{z_b z_b}$ exist in $\mathbf{C}_{\text{Aerobb}}^*$ is given by:

$$\begin{aligned} c_{z_b z_b} &= -\int_L \frac{\partial(dT)}{\partial V_y}\cos^2\beta - \int_L \frac{\partial(dT)}{\partial V_z}\sin\beta\cos\beta \\ &\quad + \int_L \frac{\partial(dS)}{\partial V_y}\cos\beta\sin\beta + \int_L \frac{\partial(dS)}{\partial V_z}\sin^2\beta \end{aligned} \tag{13}$$

in which L is the element length, and expressions of four distinct elements, which are $\frac{\partial(dT)}{\partial V_y}$, $\frac{\partial(dT)}{\partial V_z}$, $\frac{\partial(dS)}{\partial V_y}$, and $\frac{\partial(dS)}{\partial V_z}$ are given in Appendix A, and the detailed derivations for $\frac{\partial(dT)}{\partial V_y}$ are introduced in [45].

Similarly, translational forces and bending moments acting on tower top DOFs within the tower bottom coordinate system can be consolidated into vector and matrix forms:

$$\mathbf{F}_{\text{Aerot}}^* = \mathbf{F}_{\text{Aerot}}^{0*} - \begin{bmatrix} \mathbf{C}_{\text{Aerotb}}^* & \mathbf{C}_{\text{Aerott}}^* & \mathbf{C}_{\text{Aerotp}}^* \end{bmatrix} \begin{Bmatrix} \dot{\mathbf{v}}^e \\ \dot{\mathbf{u}}^{\text{top,,e}} \\ \dot{\mathbf{U}} \end{Bmatrix} \tag{14}$$

Specifically, the aerodynamic damping element corresponding to the tower top's SS motion is given as:

$$c_{y_t y_t} = N_b \int_0^R \frac{\partial(dS)}{\partial V_z} \tag{15}$$

where N_b represents the number of blades, and for the case discussed in this paper, $N_b = 3$. The upper limit R of integration indicates the radius of the rotor.

Up to this point, we have categorized the aerodynamic loads affecting both the rotor and the tower top node into two distinct groups: the static components, represented by $\mathbf{F}_{\text{Aerob}}^{0*}$ and $\mathbf{F}_{\text{Aerot}}^{0*}$, and the contributions from aerodynamic damping, which are encompassed by damping matrices such as diagonal elements $\mathbf{C}_{\text{Aerobb}}^*$ and $\mathbf{C}_{\text{Aerott}}^*$ for blade and tower top DOFs, among others.

However, we have yet to determine the aerodynamic load exerted on the floating platform due to the rotor $\mathbf{F}_{\text{Aerop}}^*$. These loads are transmitted through the tower by utilizing a transfer matrix denoted as $\mathbf{A}_{\text{pt}}$ [26].

$$\mathbf{F}_{\text{Aerop}}^* = \mathbf{A}_{\text{pt}} \mathbf{F}_{\text{Aerot}}^* \tag{16}$$

The static aerodynamic force vectors and the aero-damping matrices for platform DOFs can be readily derived. More specifically, the aerodynamic damping associated with yaw motion under standstill and yaw misalignment conditions is provided as follows:

$$c_{U_6, U_6} = \frac{N_b}{2} \int_0^R r^2 \frac{\partial(dS)}{\partial V_z} \tag{17}$$

2.3 | Hydrodynamic Damping and Mooring Lines/ Hydrostatic Stiffness

When modeling the FOWT dynamics, spar platforms have emerged as exceptionally stable support structures. Their unique attribute lies in their inherent buoyancy, characterized by hydrostatic stability. This stability remains under various operational and extreme conditions, owing to the ballast stabilization mechanism. This, in turn, shifts the focus of stability analysis from the traditional hydrostatic aspects to the more prominent influences of hydrodynamics and aerodynamics. Recent research has clarified the contribution of these dynamic effects [26]. As the foundation, Section 2.3.1 introduces the hydrodynamic damping sources, and Section 2.3.2 provides the stiffness from mooring lines, which is essential for platform surge and sway movements. Hydrostatic stiffness is also introduced in Section 2.3.2.

2.3.1 | Hydrodynamic Damping

Both the frequency and time domain analyses in this study consider the contribution of hydrodynamic force from periodic wave excitations. Hydrodynamic forces typically include viscous drag force described by Morison's equation and radiation memory effect which can be accounted for through potential flow theory [48].

The Morison's drag force at platform height Z gives:

$$\begin{aligned} dF_i^{\text{Platform}}(t, Z) &= -C_A \rho_w \left(\frac{\pi D^2}{4} dZ\right) \ddot{U}_i(Z) \\ &\quad + (1 + C_A)\rho_w \left(\frac{\pi D^2}{4} dZ\right) a_i(t, Z) \\ &\quad + \frac{1}{2} C_D \rho_w (D \cdot dZ)\left[v_i(t, Z) - \dot{U}_i(Z)\right] \\ &\quad \left[\left(v_1(t, Z) - \dot{U}_1(Z)\right)^2 + \left(v_2(t, Z) - \dot{U}_2(Z)\right)^2\right]^{\frac{1}{2}} \end{aligned} \tag{18}$$

where the coefficients C_A and C_D are the normalized hydrodynamic added-mass and viscous-drag coefficients respectively. For a spar-type platform, C_A and C_D are taken as 0.97 and 0.6 [43]. ρ_w is denoted as the seawater density, and D is the diameter of the cylinder strip, dZ is the strip height, $\ddot{U}_i(Z)$ and $\dot{U}_i(Z)$ are the strip acceleration and velocity of the ith DOF of a platform. Specifically, $\dot{U}_1(Z)$ and $\dot{U}_2(Z)$ represent the platform surge and

sway velocities respectively. v_i and a_i are the components of the undisturbed fluid-particle velocity and acceleration in the direction of ith DOF.

The memory effect is recorded through a convolution function:

$$\mathrm{d}F_{R,i}(t) = - \int_0^t h_{ij}(t-\tau)\dot{U}_j(\tau)\mathrm{d}\tau, \ i,j = 1, \dots, 6 \tag{19}$$

in which $h_{ij}(t - \tau)$ is the (i,j) component of the matrix known as the wave-radiation-retardation kernel [48]:

$$h_{ij}(t) = \frac{2}{\pi} \int_0^\infty C_{h,ij}(\omega) \cos(\omega t)\mathrm{d}\omega, \ i,j = 1, \dots, 6 \tag{20}$$

Traditionally, stability analysis methods have predominantly considered viscous hydrodynamic damping while overlooking radiation effects arising from hydrodynamics. Recent research by Li et al. [25] introduces a linear and explicit method grounded in potential flow theory to assess radiation damping. This approach complements the incorporation of viscous damping, as detailed in Meng et al.'s work based on Morison's equation [26]. Expressions for viscous and radiation damping components denoted as $\mathbf{C}_{\text{Morison}}$ and $\mathbf{C}_{\text{radia}}$ show the following form:

$$\mathbf{C}_{\text{Morison}} = \begin{bmatrix} c_{U_1 U_1}^{vis} & 0 & 0 & 0 & c_{U_1 U_5}^{vis} & 0 \\ 0 & c_{U_2 U_2}^{vis} & 0 & c_{U_2 U_4}^{vis} & 0 & 0 \\ 0 & 0 & 0 & 0 & 0 & 0 \\ 0 & c_{U_4 U_2}^{vis} & 0 & c_{U_4 U_4}^{vis} & 0 & 0 \\ c_{U_5 U_1}^{vis} & 0 & 0 & 0 & c_{U_5 U_5}^{vis} & 0 \\ 0 & 0 & 0 & 0 & 0 & 0 \end{bmatrix} \tag{21}$$

and

$$\mathbf{C}_{\text{radia}} = \begin{bmatrix} c_{U_1 U_1}^{rad} & 0 & 0 & 0 & c_{U_1 U_5}^{rad} & 0 \\ 0 & c_{U_2 U_2}^{rad} & 0 & c_{U_2 U_4}^{rad} & 0 & 0 \\ 0 & 0 & c_{U_3 U_3}^{rad} & 0 & 0 & 0 \\ 0 & c_{U_4 U_2}^{rad} & 0 & c_{U_4 U_4}^{rad} & 0 & 0 \\ c_{U_5 U_1}^{rad} & 0 & 0 & 0 & c_{U_5 U_5}^{rad} & 0 \\ 0 & 0 & 0 & 0 & 0 & 0 \end{bmatrix} \tag{22}$$

Detailed expressions for elements in these matrices can be found in Meng et al.'s reference [26].

Furthermore, it is essential to account for additional proportional damping $\mathbf{C}_{\text{add}}$, a concept defined by Jonkman et al. [43]. Collectively, these elements complement each other in the assessment of cumulative hydrodynamic damping, and it can be expressed as follows:

$$\mathbf{C}_{\text{hydro}} = \mathbf{C}_{\text{radia}} + \mathbf{C}_{\text{Morison}} + \mathbf{C}_{\text{add}} \tag{23}$$

2.3.2 | Mooring Line and Hydrostatic Stiffness

In addition to hydrodynamic considerations, the mooring lines associated with spar platform introduce nonlinear stiffness. The platform's perturbed position influences this nonlinearity. The author's prior research [26] and the NREL technical report [43] confirm the nonlinear behavior of mooring line loads when the platform follows a linear trajectory in specific directions. To ensure precision in analysis, one should ideally determine mooring line stiffness values relative to the static balanced position. However, the platform can be assumed to be placed in an undisturbed position for practical reasons. The calibration of mooring stiffness is facilitated by using OpenMOOR, an open-source tool developed by Chen et al. [49]. The resulting calibrated stiffness matrix is a 6×6 matrix:

$$\mathbf{K}_{\text{moor}} = \begin{bmatrix} K_{moor}^{11} & 0 & 0 & 0 & K_{moor}^{15} & 0 \\ 0 & K_{moor}^{22} & 0 & K_{moor}^{24} & 0 & 0 \\ 0 & 0 & K_{moor}^{33} & 0 & 0 & 0 \\ 0 & K_{moor}^{42} & 0 & K_{moor}^{44} & 0 & 0 \\ K_{moor}^{51} & 0 & 0 & 0 & K_{moor}^{55} & 0 \\ 0 & 0 & 0 & 0 & 0 & K_{moor}^{66} \end{bmatrix} \tag{24}$$

with the specific matrix elements detailed in Meng et al.'s work [26].

Besides, the spar-type platform is an unconditional stable system attributed to hydrostatic stiffness, it gives [46]:

$$\mathbf{K}_{\text{buoy}} = \begin{bmatrix} 0 & 0 & 0 & 0 & 0 & 0 \\ 0 & 0 & 0 & 0 & 0 & 0 \\ 0 & 0 & \rho_w g A_0 & 0 & -\rho_w g \iint_{A_0} X\,\mathrm{d}A & 0 \\ 0 & 0 & 0 & \rho_w g \iint_{A_0} Y^2\,\mathrm{d}A + \rho_w g V_w Z_{GB} & 0 & 0 \\ 0 & 0 & -\rho_w g \iint_{A_0} X\,\mathrm{d}A & 0 & \rho_w g \iint_{A_0} X^2\,\mathrm{d}A + \rho_w g V_w Z_{GB} & 0 \\ 0 & 0 & 0 & 0 & 0 & 0 \end{bmatrix} \tag{25}$$

in which, A_0 is the water-plane area of the support platform when it is in its undisplaced position, and Z_{GB} is the metacentric height.

Thus, the overall stiffness matrix for platform shows:

$$\mathbf{K} = \mathbf{K}_{\text{buoy}} + \mathbf{K}_{\text{moor}} \tag{26}$$

2.4 | State-Space Method

Once the system matrices have been identified, one can determine damping ratios for each mode through complex modal analysis in state space, as outlined in the work by Craig [50]. This approach involves calculating the eigenvalues of a first-order differential equation to extract the damping ratios. The reduced-order differential equation can be expressed as follows:

$$\mathbf{A}\dot{z}(t) + \mathbf{B}z(t) = \mathbf{0} \tag{27}$$

here, the matrices $\mathbf{A}$ and $\mathbf{B}$ are assembled as:

$$\mathbf{A} = \begin{bmatrix} \mathbf{C} & \mathbf{M} \\ \mathbf{M} & \mathbf{0} \end{bmatrix}, \mathbf{B} = \begin{bmatrix} \mathbf{K} & \mathbf{0} \\ \mathbf{0} & -\mathbf{M} \end{bmatrix} \tag{28}$$

in which the damping matrix $\mathbf{C}$ and stiffness matrix $\mathbf{K}$ contain the aerodynamic damping, hydrodynamic damping, and mooring line and hydrostatic stiffness introduced in Sections 2.2 and 2.3.

We can obtain the following generalized algebraic eigenvalue equation:

$$[\lambda \mathbf{A} + \mathbf{B}]\theta = \mathbf{0} \tag{29}$$

The solution of this eigenvalue problem consists of eigenvalues λ_n, and corresponding eigenvectors θ_n. The eigenvalues must satisfy the characteristic equation:

$$\det(\lambda \mathbf{A} + \mathbf{B}) = 0 \tag{30}$$

each complex eigenvalue λ_n for the nth mode takes the form:

$$\lambda_n = -\zeta_n \omega_n + i\omega_n\sqrt{1 - \zeta_n^2} \tag{31}$$

where ω_n represents the undamped natural frequency of the nth mode, and ζ_n is the corresponding damping ratio. By substituting λ_n into Equation (29), the eigenvector can be further determined. The eigenvector describes the mode shape in structural dynamic analysis. Natural frequency and mode shape can be used to identify a mode.

For the state-space method to be applied effectively, the matrices $\mathbf{A}$ and $\mathbf{B}$ must remain time-independent, meaning they should be constant matrices throughout the analysis.

2.5 | VGs Installation

VGs are traditionally installed in the inboard sections to enhance AEP, depicted in Figure 3 as arrows in red. In this study, VGs are equipped in outboard sections following blue arrows. To better determine the VGs configuration, at least six parameters must be proposed: $h_{VG}^{i,k}, l_{VG}^{i,k}, \alpha_{VG}^{i,k}, xVG_1^{i,k}/c, xVG_2^{i,k}/c, xVG_3^{i,k}/c$. The first three parameters represent the VGs normalized height, length, and angle, respectively. They are constrained such that $h_{VG}^{i,k} \in [0.007, 0.025]$, $l_{VG}^{i,k} \in [0.02, 0.05]$, and $\alpha_{VG}^{i,k} \in [10°, 15°]$. Besides, VGs are designed to be mounted uniformly along the blade length direction, as shown in Figure 3 (right). We set the constraint that VGs obey quadratic function distribution along the blade length. According to the fundamental mathematics, three points should be given to determine the para-curve exclusively, those being $xVG_1^{i,k}/c, xVG_2^{i,k}/c, xVG_3^{i,k}/c$ respectively. xVG/c represents the ratio of a VG coordinate to blade chord length c at the blade chord direction, and subscripts 1–3 are denoted for the installation region's start, middle, and end points along the blade length direction. In practice, the VG array line is also controlled by another constraint condition of $xVG/c \in [0.2, 0.5]$.

2.6 | Particle Swarm Optimization Method

As introduced, this paper devotes itself to developing the VGs usage in stability enhancement. The following VG optimization will be initially conducted using the PSO method. The PSO algorithm is developed based on the particle concept, inspired by
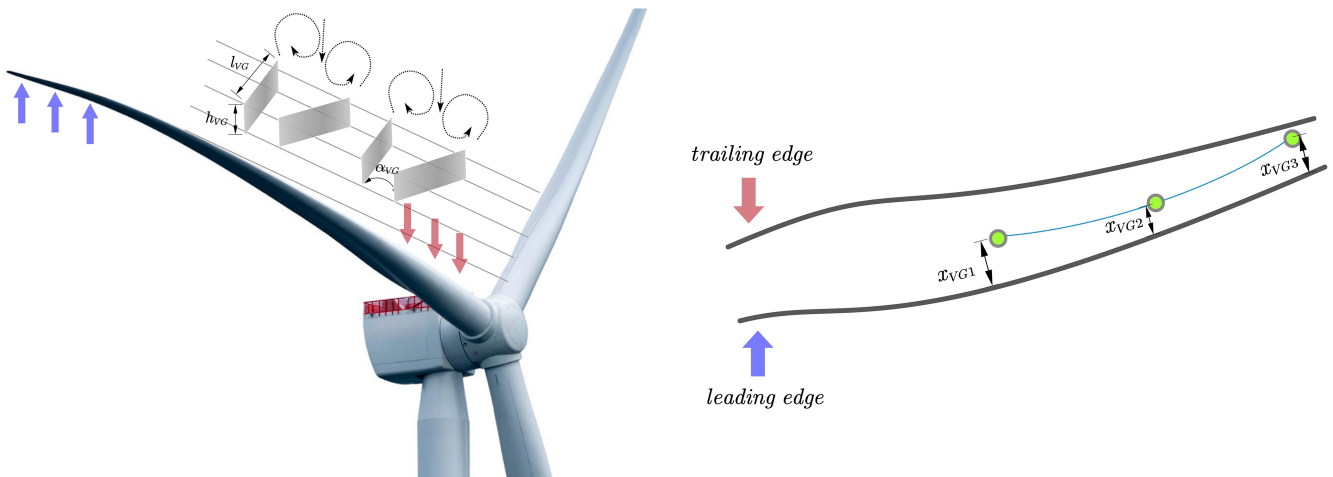
FIGURE 3 | Illustration of VG installation on a blade to mitigate stall-induced instability.

the social behavior of birds or schools of fish. Its nature is to give a bunch of particles randomly, and each particle is endowed with random values for two characteristics: position $\mathbf{x}_i^t$ and velocity $\mathbf{v}_i^t$. $f(\mathbf{x}_i^k)$ is the objective function (also called fitness value typically). It could be an explicit or implicit function concerning position $\mathbf{x}_i^t$, $\mathbf{v}_i^t$ provides propulsive velocity for $\mathbf{x}_i^t$ to obtain the optimized solution. Each particle moves towards its prior personal best position ($\mathbf{p}_{\text{best}}^t$) and the global best position ($\mathbf{g}_{\text{best}}^t$) in the swarm, their definitions can be expressed by (for a maximization problem) [51]:

$$\mathbf{p}_{\text{best}_i}^t = \mathbf{x}_i^* | f(\mathbf{x}_i^*) = \max_{k=1,2,\ldots,t}\left(\left\{f(\mathbf{x}_i^k)\right\}\right) \tag{32}$$

where $i \in [1, N]$, and

$$\mathbf{g}_{\text{best}}^t = \mathbf{x}_*^t | f(\mathbf{x}_*^t) = \max_{i=1,2,\ldots,N;k=1,2,\ldots,t}\left(\left\{f(\mathbf{x}_i^k)\right\}\right) \tag{33}$$

in which t represents the tth generation of iteration and i represents the ith particle among the particle swarm; in addition, N implies that there are totally N particles in the swarm; in this paper, $N = 100$.

Particle positions $\mathbf{x}_i^{t+1}$ update automatically at time $t + 1$ by adding the velocity vector $\mathbf{v}_i^{t+1}$ to the states $\mathbf{x}_i^t$ at the last step:

$$\begin{aligned} \mathbf{v}_i^{t+1} &= \omega\mathbf{v}_i^t + c_1 r_1\left(\mathbf{p}_{\text{best}_i}^t - \mathbf{x}_i^t\right) + c_2 r_2\left(\mathbf{g}_{\text{best}}^t - \mathbf{x}_i^t\right) \\ \mathbf{x}_i^{t+1} &= \mathbf{x}_i^t + \mathbf{v}_i^{t+1} \end{aligned} \tag{34}$$

where ω (taken as 0.5) is the inertia weight utilized to balance local exploitation and global exploration, r_1 and r_2 are random values uniformly distributed within the range of $[0,1]$, and c_1 and c_2 are called "acceleration coefficients" and they are given as 1.5 in this study.

Equation (34) explains the inside principle of the PSO method: particle positions move towards both the personally and globally optimal positions, also controlled by their velocity inertia, and Figure 4 vividly shows this process [52].

It is important to acknowledge that the fitness in this study is given by:
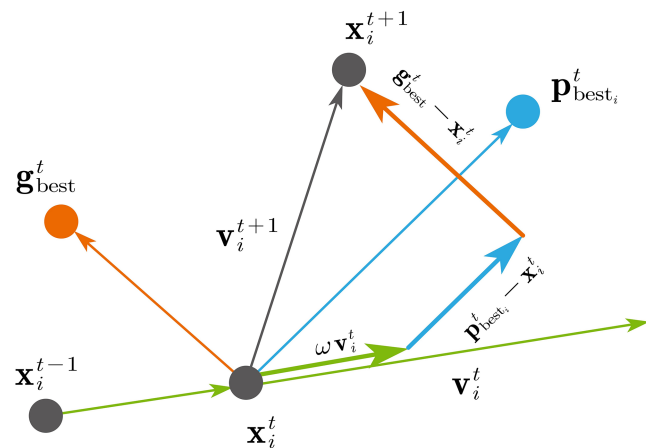

FIGURE 4 | PSO algorithm mechanism.

$$f(\mathbf{x}_i^k) = \max\left(\chi | \left\{\zeta_i(\chi) = -\zeta_{cri}(\chi)\right\}\right) \tag{35}$$

and

$$\mathbf{x}_i^k = [h_{VG}^{i,k}, l_{VG}^{i,k}, \alpha_{VG}^{i,k}, xVG_1^{i,k}/c, xVG_2^{i,k}/c, xVG_3^{i,k}/c] \tag{36}$$

in which ζ_i is the damping ratio for a given mode, and its value is based on the updated lift and drag coefficients using XFoilVG [41], and the damping ratios are determined through the state space method in Section 2.4. We propose ζ_{cri} as the critical damping ratio which equals to structural damping ratio in value. ζ_{cri} is seen as the criterion in judging instability, and when $\zeta_i < -\zeta_{cri}$, instability occurs. Ultimately, the whole process for the optimization is summarized in Figure 5. It firstly sets up initial ranges for the six parameters introduced above and then generates N particles; consequently, determines aerodynamic polar utilizing XFoilVG; and afterward adopts the state space method in Section 2.4 and dichotomy to find the yaw misalignment angle χ that meets the requirement of $\zeta_i = -\zeta_{cri}$. Then, the judgment is made as to whether the objective can be achieved if satisfied; otherwise, regenerate a new swarm and restart the loop.

3 | Primary Results on Stability

This section presents the primary stability analysis results for a clean 5 MW rotor, specifically focusing on the platform yaw, 1st order tower SS, and the third first-order rotor edgewise modes. The modal analysis treats the entire wind turbine as a global system. As a result, there are three first-order rotor edgewise modes. This paper focuses on the third 1st order mode, as it exhibits the widest range of negative aerodynamic damping, indicating it faces the greatest risk. The third first-order rotor edgewise mode shape and its corresponding frequency are illustrated in Figure 6. This mode shape corresponds to the 14th mode of the overall FOWT system, with a frequency of 1.087 Hz. Notably, the mode shape is asymmetric. These particular modes have been singled out for detailed examination due to substantial evidence demonstrating their heightened vulnerability to stall-induced aerodynamic instability [10]. Figure 7 highlights the potential aerodynamic instability risks associated with these modes. In this situation, wind speed $V_0 = 50$ m/s, azimuth angle $\Psi = 0°$, represents the first blade points upward, which is a typical configuration, and yaw misalignment angle $\chi = [-180°, 180°]$. Platform yaw, tower top SS, and the third first-order rotor edgewise motion exhibit significant risk to aerodynamic instability, primarily driven by negative aerodynamic damping effects. Table 1 presents the damping ratios resulting from the hydrodynamic contribution on platform yaw mode, even when accounting for the hydrodynamic damping effect (4.34%), the overall damping in the platform yaw mode may appear positive but is still considered unstable in engineering. Hence, this paper focuses on these three critical modes to enhance their stability characteristics. The objective is to devise strategies and solutions to mitigate stall-induced aerodynamic instability and ensure the system's reliable and safe operation.

Moreover, in a pie chart, Figure 8 provides aerodynamic damping $\int_L \frac{\partial(\mathrm{d}S)}{\partial V_z}$ and modal damping $\int_L \frac{\partial(\mathrm{d}S)}{\partial V_z}\phi^2(x)$ values for each blade
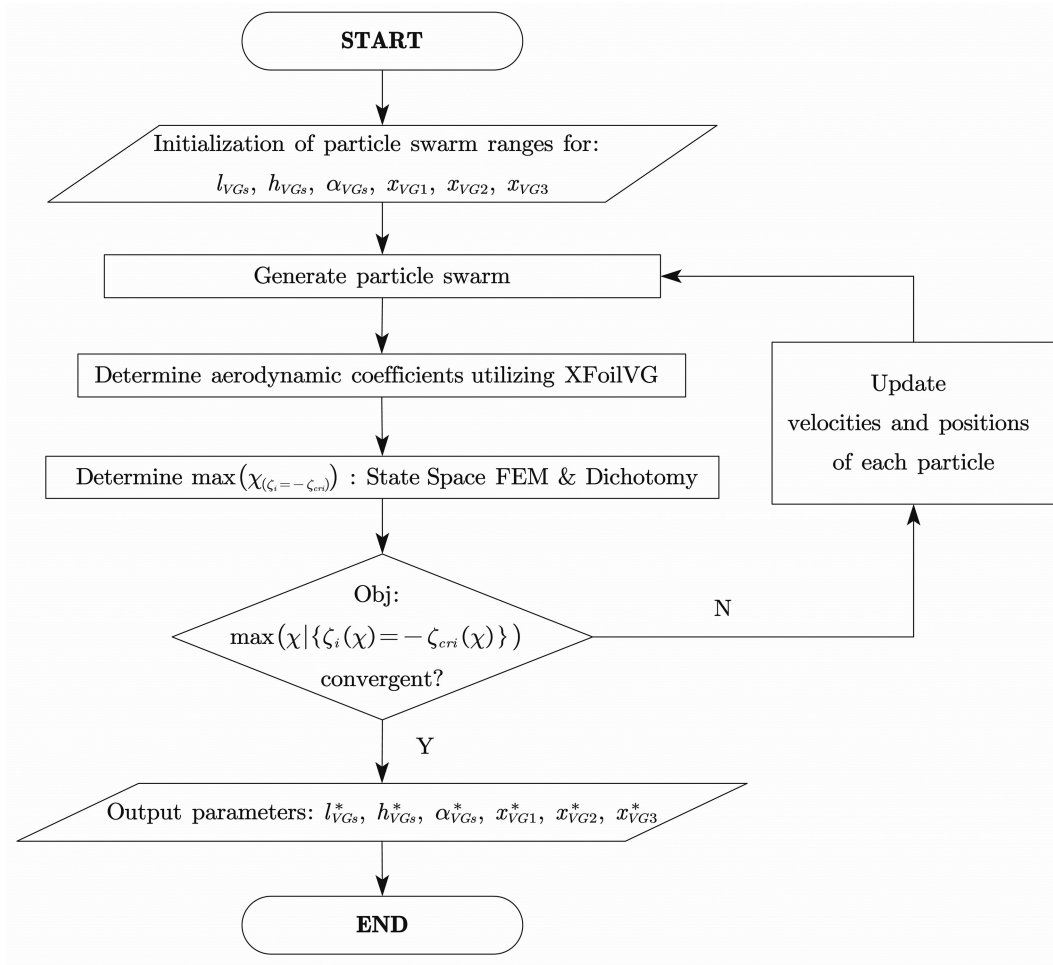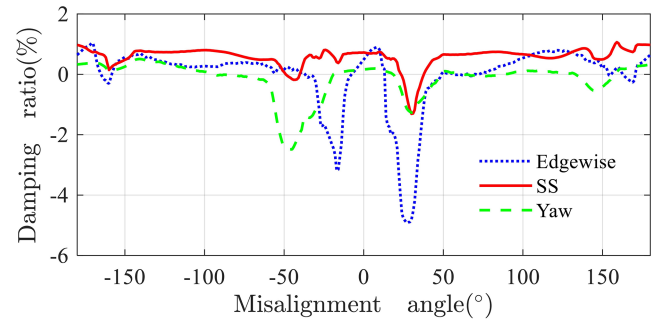
FIGURE 5 | Flowchart of the PSO method for VG configuration optimization in mitigating instability.
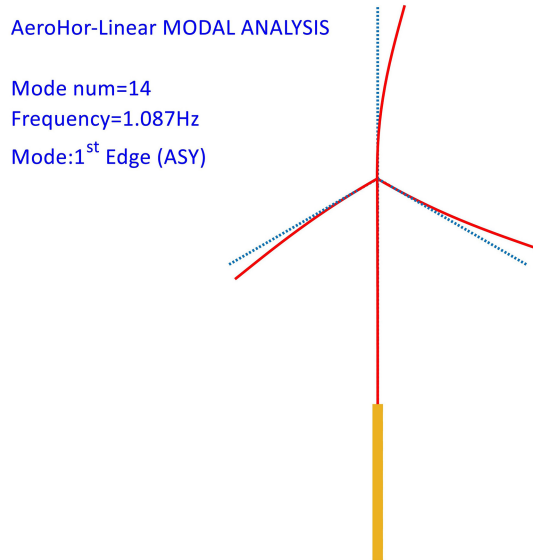
**FIGURE 6** | The third first-order rotor edgewise mode shape and frequency.

FIGURE 7 | Aerodynamic damping ratios for NREL OC3 5 MW standstill wind turbine edgewise, SS, and yaw modes with wind speed $V_0 = 50$ m/s, azimuth angle $\Psi = 0°$, yaw misalignment angle $\chi = [-180°, 180°]$.

section. This graphical representation illustrates the distribution of negative aerodynamic damping and modal damping along the blade (in the radial direction), and along the yaw misalignment angle between the inflow and rotor plane (in the azimuthal direction). While it is evident that negative aerodynamic damping primarily manifests in the inboard sections of the blade (Figure 8a), it is noteworthy that the outboard sections play a significant role in contributing to the overall negative modal damping for a specific mode (Figure 8b). This observation underscores the critical importance of the outboard sections as a significant source of negative aerodynamic damping for a given mode.

This study serves as a proof-of-concept using a quasi-steady framework. As noted by Wang et al. [18], dynamic stall significantly

TABLE 1 | Hydrodynamic damping ratios (wave height = 5 m, wave period = 9.6 s).

Damping ratio values (%)	Radiation	Morison's viscous	Additional	Overall
Yaw mode	—	—	4.34	4.34

(a) edgewise aerodynamic damping coefficient   (b) edgewise modal damping coefficient
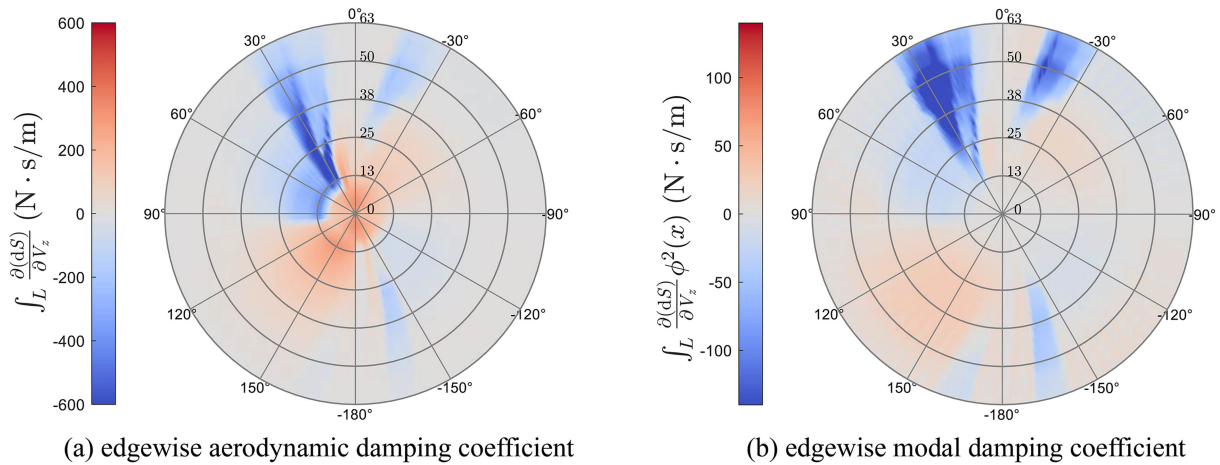
FIGURE 8 | Edgewise aerodynamic damping coefficient: $\int_L \frac{\partial(dS)}{\partial V_z}$ (a) and modal damping coefficient $\int_L \frac{\partial(dS)}{\partial V_z} \phi^2(x)$ (wind speed $V_0 = 50$ m/s, yaw misalignment angle $\chi = [-180°, 180°]$).
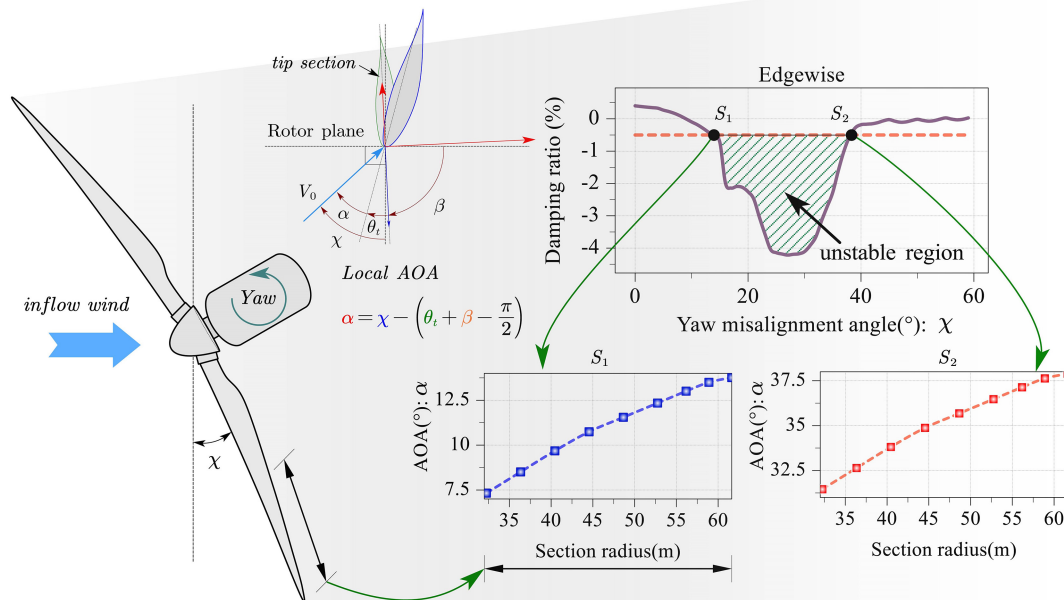

FIGURE 9 | Illustration of the mechanism of stability enhancement using VGs.

affects instability, underscoring the need to assess the effectiveness of VGs in delaying stall-induced instability under dynamic conditions. However, our preliminary study shows that instability is sensitive to different choices of dynamic stall models and even to different implementations of the same dynamic stall model [53]. Furthermore, no dynamic stall model has been validated for the larger AoA tested in this work. Thus, this paper does not consider the effects of dynamic stall. Future work will quantify the effects of VGs, incorporating dynamic stall models, or even using the middle-fidelity vortex models proposed by Yu et al. [54].

4 | Stability Enhancement Using Vortex Generators

4.1 | Inspiration

According to Figure 8b, outboard airfoil sections highly contribute to the total modal damping, whereas the corresponding local AoA values when azimuth angle equals 0 for outboard sections at S_1 and S_2 can be seen in Figure 9. S_1 and S_2 are two yaw misalignment angle points controlling the instability region for
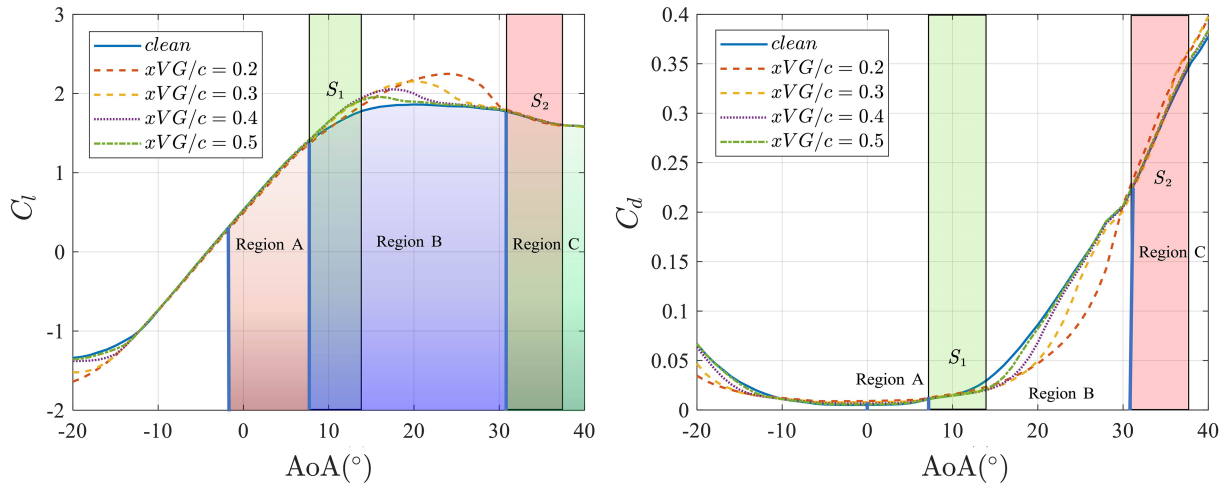
FIGURE 10 | C_l and C_d polars of a clean and VGs mounted-blade section(DU 93-W-210), generated by XFoilVG.

edgewise movement. Yaw misalignment angles between S_1 and S_2 result in negative damping when structural damping is subtracted, indicating that the system is at a high risk of instability. Among these two points, S_1 corresponds to the local AoA of outboard sections from 7.326° to 13.764°. In contrast, the right point S_2 corresponds to the local AoA from 31.456 to 37.894°.

AoA ranges concerning S_1 and S_2 are shown in Figure 10, from which we can find that S_1 and S_2 corresponding AoA ranges are mainly located in Region B and Region C, respectively. Figure 10 shows the C_l and C_d results for a variety of VG arrangements, highlighting the differences observed in Region B after the VGs were mounted on a specific blade spanwise position, while negligible influences are observed in Regions A and C. The findings above indicate that no matter how we arrange the VGs on an airfoil, its S_2 hardly be changed, while the value of S_1 can be modified as the related C_l and C_d data for S_1 mainly come from Region B. This feature allows us to push the stall-induced instability backward and keep the S_2 stationary. Therefore, the authors decided to deploy VGs at the outboard sections, enabling the postponement of stall onset (S_1 can be delayed as it resides in Region B).

The core question to be answered in this paper is how to arrange VGs that can reduce the negative damping region the most. The authors introduce a widely used intelligence PSO algorithm in the sub-section below. Based on the optimization results from the PSO method and the nature behind the results, the authors propose one kind of FO method (newly developed in this paper) to obtain reasonable solutions for VG installation in improving the performance of delaying stall-induced instability on a 5 MW wind turbine. Finally, we implemented the FO method on the IEA 15 MW reference wind turbine [44]. Sections 4.2 and 4.3 propose PSO and FO methods for determining the optimal distribution for VGs, respectively, and both of them are studied with an NREL 5 MW model; Section 4.4 is proposed to show responses based on nonlinear aerodynamic theory (introduced in Ref [45]) and validate the results from the linearized model in the frequency domain; Section 4.5 performs these two methods implementation on an IEA 15MW wind turbine to demonstrate the effectiveness of the proposed approach on different sizes of wind turbines. Additionally, the following optimization takes the value of the

azimuth angle as 0, and the influence of the azimuth angle will be discussed in Section 5.1.

4.2 | Particle Swarm Optimization

This subsection adopts the PSO algorithm introduced in Section 2.6 to optimize VG installations. Two cases (Case1 and Case2 in Figure 11, the dotted circles indicate the radial position on the blade where VGs are installed, extending from this point to the blade's tip. The arrows indicate the installation range of the VGs.) are proposed as implementation examples. Case 1 uses fewer VGs, starting from a distance of approximately 40 m from the hub and installing them all the way to the blade tip, which is located 63 m from the hub. In contrast, Case 2 uses more VGs, starting from a distance of 29 m from the hub and also extending to the blade tip at the same 63 m position. This test is designed to visualize the stability enhancement effect of installing varying amounts of VGs. Case1 and Case2 converge after around 15 iterations, whereas Case2 is superior to Case1, as more VGs are mounted. The onset of stall-induced instability angle grows from 13.87° to 19.07° and 20.08°, respectively. Particle fitness (stall angle) values change with iterations, and several iteration outcomes are shown on the right of Figure 11. The PSO algorithm produces N fitness values at each step, and all particle fitness values move towards the convergence direction and finally gather into a line. Moreover, Table 2 lists the parameters to be optimized and their optimized results for Case 2. It is demonstrated that the first three parameters tend to converge near the maximum boundary (h_{VG} reaches 0.025, given the optimization range of [0.007,0.025]; l_{VG} is optimized to 0.05, given the range of [0.02,0.05]; and α_{VG} is optimized to 15°, within the range of [10°,15°]). However, the trend for the last three parameters, xVG_i, does not appear intuitive. Section 4.3 aims to uncover the mechanisms behind this issue and propose a new approach.
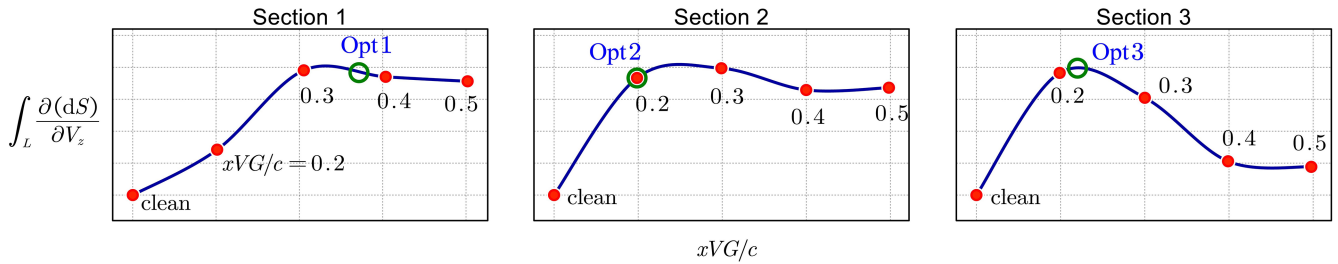
4.3 | Fast Optimization

As Equations (11) and (13) show, the edgewise stability performance mainly depends on the element $c_{z_b z_b}$, as to a parked wind
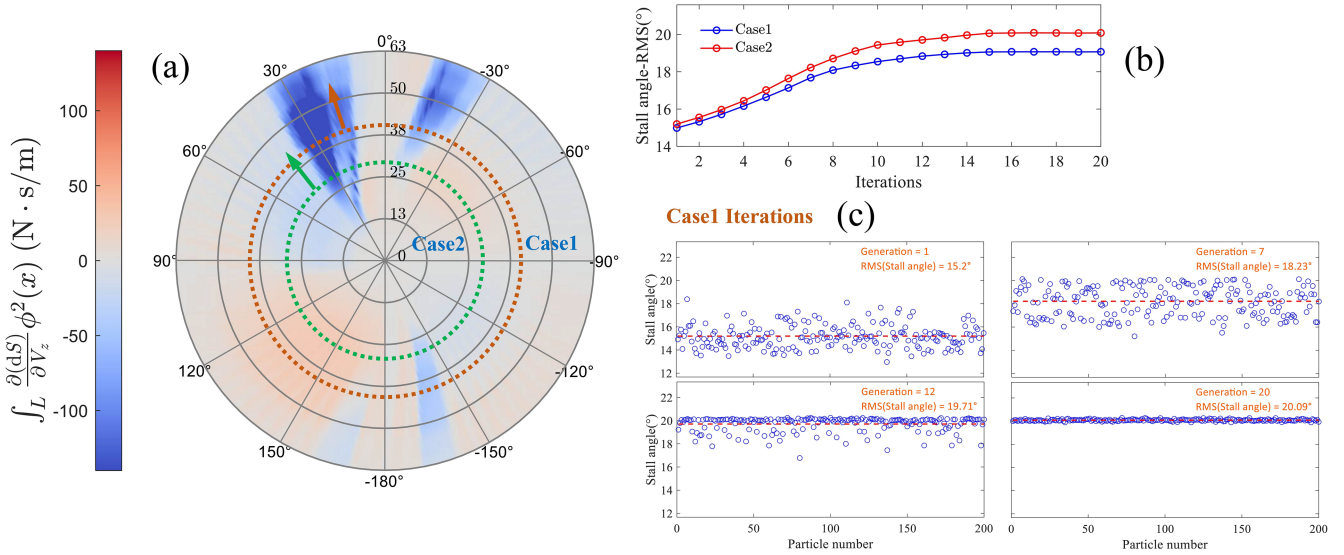
FIGURE 11 | Optimized results for edgewise instability enhancement. (a) Configuration of VGs. (b) Optimization effect. (c) Case iterations.

TABLE 2 | PSO parameter ranges and optimization results.

Parameters	h_{VG}	l_{VG}	$\alpha_{VG}(°)$	xVG_1	xVG_2	xVG_3
Given ranges	[0.007,0.025]	[0.02,0.05]	[10,15]	[0.2,0.5]	[0.2,0.5]	[0.2,0.5]
Optimization results	0.025	0.05	15	0.37	0.2	0.213

FIGURE 12 | PSO-based optimization results and their locations within the $\int_L \frac{\partial(\mathrm{d}S)}{\partial V_z}$ curve.

turbine case, its expression is given as Equation (13), and its value equals to $\int_L \frac{\partial(\mathrm{d}S)}{\partial V_z}$ as long as the rotor is well pitched (pitch angle $\beta = 90°$). Thus, the stability optimization problem can be transferred to a maximum value determination problem for $\int_L \frac{\partial(\mathrm{d}S)}{\partial V_z}$. Section 4.2 conducts an optimization procedure using the PSO method and finally finds the best solutions for the three parameters of xVG_1/c, xVG_2/c, and xVG_3/c. The results and their locations are shown in Figure 12 with the y axis being the value of $\int_L \frac{\partial(\mathrm{d}S)}{\partial V_z}$, which is a function concerning xVG/c. Although somewhat misaligned, the optimized parameters are located in the maximum region of $\int_L \frac{\partial(\mathrm{d}S)}{\partial V_z}$, proving the correctness of the conjecture mentioned above.

Besides, according to the expression of Equation (13), the value of $\int_L \frac{\partial(\mathrm{d}S)}{\partial V_z}$ can be determined based on known values of C_l, C_d, and α, among which the C_l and C_d tables are given utilizing XFoilVG. Using XFoilVG, one can retrieve data sets for C_l and C_d, provided that the airfoil coordinates data and VGs parameters are furnished as input files. In addition, local α is a function with respect to yaw misalignment angle χ and blade section parameters (θ_t and β, typically, $\beta = 90°$). χ is taken as a value that

corresponds to the misalignment angle where the stall-induced instability occurs. Finally, the problem now becomes

Inputs: $C_l \& C_d$; θ_t; ($h_{VG}, l_{VG}, \alpha_{VG}$, and x_{VG}/c)

**Outputs**: $\int_L \frac{\partial(\mathrm{d}S)}{\partial V_z}$

The first two input parameters are fixed for a specific airfoil at a radius of r, and $h_{VG}, l_{VG}, \alpha_{VG}$ tend to be the maximum values within a defined domain. In other words, the problem now should be: Find a value of x_{VG}/c for a given blade section at position r to let the value of $\int_L \frac{\partial(\mathrm{d}S)}{\partial V_z}$ maximum. This method is defined as the Fast Optimization method. More concisely:

$$\mathbf{X} : \text{at position } r (C_l \& C_d) \Rightarrow \mathbf{Y} : \text{find a } x_{VG}/c$$
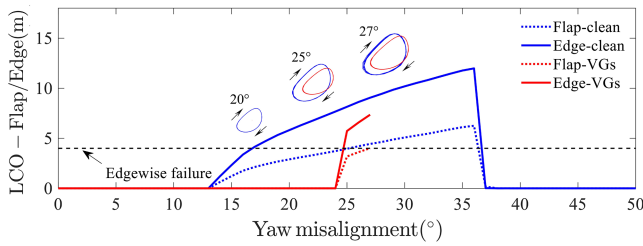$$\Rightarrow \mathbf{Z} : \text{let} \int_L \frac{\partial(\mathrm{d}S)}{\partial V_z} \text{ maximum}$$

Figure 13 shows the optimization results for Case2 employing the FO method. From Figure 13, one can find an optimized
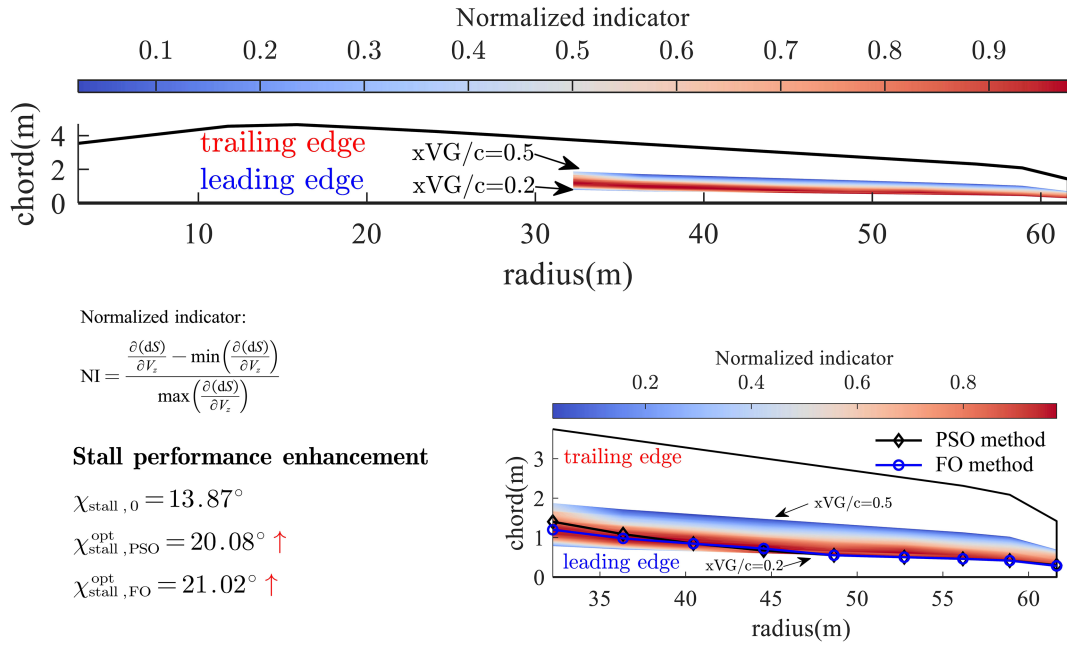
FIGURE 13 | Edgewise stability enhancement optimization results based on the PSO and FO method for NREL 5 MW wind turbine.

FIGURE 14 | VGs effect demonstration regarding yaw misalignment angle: LCOs amplitudes of blade tip section at the yaw misalignment angles: $\chi = 0° - 50°$ with the inflow wind speed of $V_0 = 50$ m/s, collective pitch angle $\beta = 90°$.

value of x_{VG}/c to let the $\int_L \frac{\partial(dS)}{\partial V_z}$ reach its maximum value for a given blade section. This method is called Fast Optimization as it reduces the computational expense compared to the PSO method. The PSO method is computationally expensive because of the "swarm" and step-by-step iterations. Moreover, optimization results from the PSO method and FO method are very close, and, surprisingly, the FO method determines a better solution to let the stall-induced instability occurrence angle range reduced from $13.87°$–$37.95°$ to $21.02°$–$37.95°$ (performance increased by 29.69%) partly because the FO approach releases the constraint of quadratic distribution of $xVG/c \in [0.2, 0.5]$ in PSO.

4.4 | Time Domain Validation

To validate the improvement in the stability of wind turbines with VGs mounted at blade tips, this section adopts a nonlinear aerodynamic model (introduced in Ref [45]) to simulate the limit cycle oscillation (LCO) amplitudes of FOWTs with and without VGs, as shown in Figure 14. In this figure, "Edgewise failure" refers to damage to the blade caused by internal forces resulting from large edgewise vibrations. The

figure reveals that after VG installation, the onset of instability is indeed delayed as expected. The onset of instability is postponed to approximately a yaw angle of $24°$. However, after VG installation, the instability exhibits unique characteristics: once entering the instability region, the amplitude growth of the steady-state vibration loop becomes more pronounced. This can be attributed to the fact that, although VG helps extend the linear region of the lift curve, the stall also happens more sharply.

Furthermore, due to the dependence of high yaw angle calculation data on the lift and drag coefficient data at high angles of attack, the data beyond $27°$ is discarded since XFoilVG can only calculate data within a limited range of AoA. Although the use of Viterna extrapolation [55] could provide reasonable lift and drag curve data, it is unnecessary because, beyond $27°$, the edgewise vibration amplitude of the blade exceeds a remarkable 5 m. Therefore, calculating its amplitude in this region has no practical significance since the blade is already damaged due to the overlarge stress at the blade root sections.

Finally, a comparison of the time-domain response is performed. Figure 15 illustrates the flapwise and edgewise time responses of the wind turbine blades at a yaw angle of $17°$, wind speed of 50 m/s, and a pitch angle of $90°$. It is evident that the clean blade eventually reaches an LCO in a steady state, while the blades with VGs quickly dampen. Furthermore, it is apparent that the flapwise static equilibrium position of the blades with VGs is higher, which is a result of the VGs lifting the lift coefficient polar. This indicates that the VG-equipped blade can increase the load. However, as long as the load remains within the allowable range, it is still considered acceptable. According to the left image in Figure 15, the displacement of the blade with VGs is only about 10% greater than the maximum value of the clean one. Nevertheless, this is a significant consideration in real-world applications, and designers may need to evaluate this aspect more carefully.
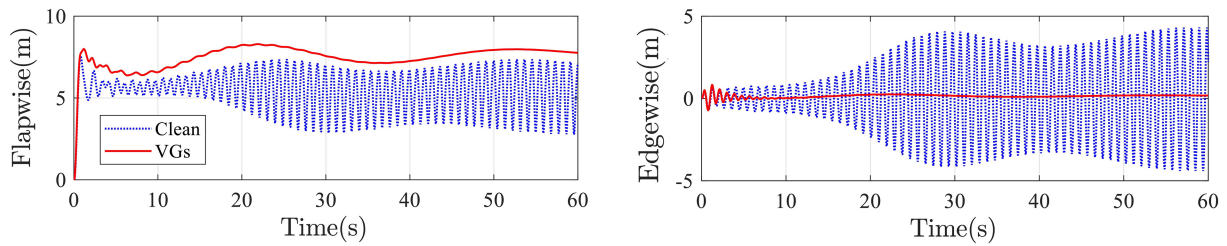
FIGURE 15 | VGs effects demonstration: displacements at blade tip section in time domain, yaw misalignment angle $\chi = 17°$, wind speed $V_0 = 50$ m/s, collective pitch angle $\beta = 90°$.

4.5 | Effects of VGs on the IEA 15 MW Wind Turbine

The proposed idea is extended to applying the IEA 15 MW wind turbine model [44]. The IEA 15 MW wind turbine is a three-rotor horizontal wind turbine with a rotor diameter of 240 m and a towering hub height of 150 m. To evaluate the effectiveness and robustness of the methodology put forth in this paper, the method is applied to the 15 MW wind turbine rotor. Table 3 provides both the flapwise and edgewise frequencies as reported by the IEA and as determined in this paper. For the 1st flapwise mode frequency, the IEA reference value is 0.555 Hz, while the calculated value in this study is 0.5566 Hz, resulting in a relative error of 0.28%. Similarly, for the 1st edgewise frequency, the IEA reference is 0.642 Hz, and the calculated value is 0.6385 Hz, with a relative error of 0.545%. These results indicate that the dynamic characteristics of the integrated model closely align with the data outlined in the official definition report.

One key aspect that merits attention is the modal damping map, illustrated in Figure 16a. A detailed observation of the contour plot reveals that the installation of VGs is optimally effective when placed at an approximately spanwise location of 72 m. Figure 17 provides additional compelling evidence of the method's effectiveness when applied to the 15 MW wind turbine: An instability assessment using the FO method showcases a substantial delay in the onset of instability, with the instability angle range narrowing from 11.39° to 32.96° in an uncontrolled scenario to 16.18°–32.96° with VGs installed. This remarkable 28.55% improvement demonstrates the method's suitability for larger wind turbines, emphasizing its robustness in applications. Furthermore, Figure 16b confirms the effectiveness by illustrating a noteworthy backward shift in the deep negative damping region following the installation of VGs. This shift significantly improves the wind turbine's aerodynamic performance and overall stability.

To provide a meaningful point of comparison, the study juxtaposes the stall angle of the 15 MW wind turbine with that of a 5 MW wind turbine. This contrast emphasizes the heightened risk of stall-induced instability in larger wind turbines. Table 4 summarizes the optimization results of the instability angle for both the NREL 5 MW and IEA 15 MW wind turbines, following the implementation of VGs. For the NREL 5 MW turbine, the instability angle without VGs ranges from 13.87°–37.95°. With VGs optimized using the PSO method, the instability angle improves to 20.08°–37.95°, representing a 25.79% improvement, while the FO method further enhances

TABLE 3 | Natural frequencies for IEA 15 MW wind turbine, comparison between FAST and AeroHor (model in this paper).

Frequencies (Hz)	1st Flap	1st Edge
IEA Reference	0.555	0.642
AeroHor	0.5566	0.6385
Error	0.28%	0.545%

it to 21.02°–37.95°, achieving a 29.69% improvement. For the IEA 15 MW turbine, the instability angle without VGs spans 11.39°–32.26°. After applying VGs, both the PSO and FO methods improve the range to 16.18°–32.26°, yielding a consistent improvement of 22.95%.

5 | Discussions

### 5.1 | The Effects of Different Azimuthal Positions

This subsection aims to discuss the impact of the azimuth angle when performing VG array configuration optimization. Based on the preceding discussion, the azimuth angle can influence the effective yaw misalignment angle, as expressed in Equations (4) and (5), and Section 4.1 clarifies that the azimuth angle is set to 0 for the optimization discussed earlier. Figure 18 illustrates how the azimuth angle influences damping ratios. The figure shows that the region of negative damping ratios for the third first-order rotor edgewise is influenced jointly by azimuth and yaw misalignment angles. Notably, when the azimuth angle is below 90°, higher azimuth angles correspond to larger yaw misalignment angles at the onset of instability.

We further track instances where damping ratios fall below -0.5%, and plot them as the envelope in Figure 18. We extract the envelope and label the corresponding yaw misalignment angle as χ'_{stall}, and it is shown on the left of Figure 19. χ'_{stall} indicates rotor-level inflow angles that trigger the instability. However, in VG configuration optimization, the FO method employs the AoA at airfoil level. Consequently, χ'_{stall} corresponds to airfoil-class AoA α'_{stall} under the assumptions of $\beta = 0$ and $\theta_t = 0$, as shown on the right of Figure 19 (where α'_{stall} does not denote the static stall angle of the airfoil polar).

It is observed that although χ'_{stall} increases with azimuth angle when $\Psi < 78°$, α'_{stall} remains almost constant. This trend persists for various cases of $\theta_t \neq 0$ (not shown). Additionally, a similar
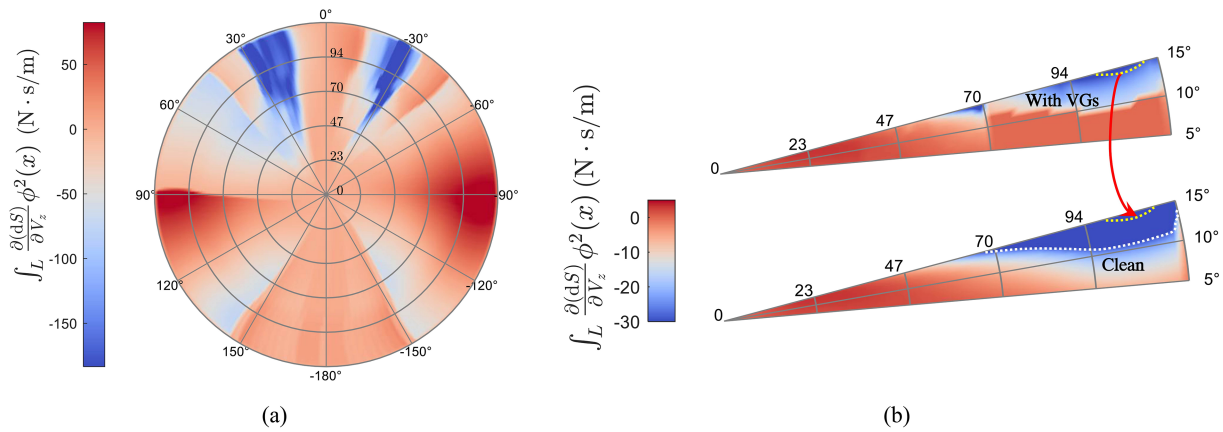
FIGURE 16 | Modal damping distribution for a 15 MW wind turbine edgewise mode (a) and VGs' contribution in delaying deep negative values of modal damping (b).
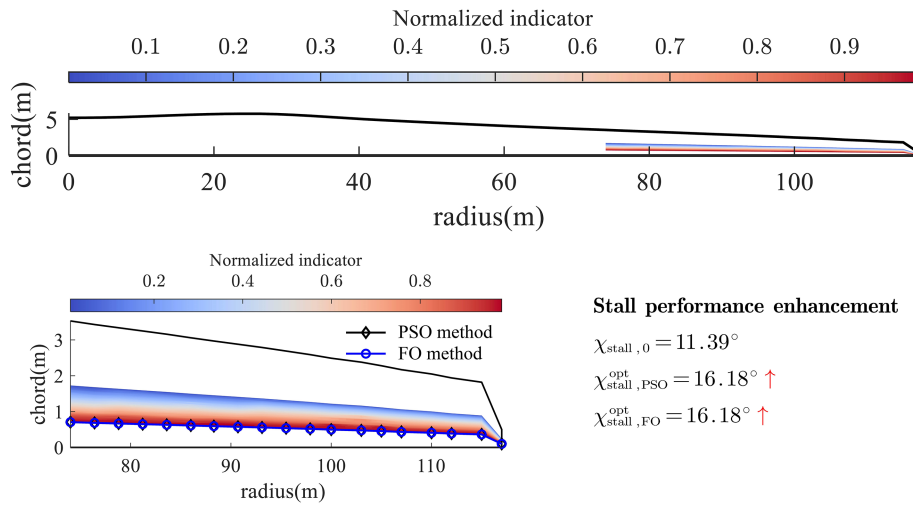
FIGURE 17 | Edgewise stability enhancement optimization based on PSO and FO methods for a 15 MW wind turbine.

TABLE 4 | The optimization results of edgewise stability performance through the implementation of VGs using PSO and FO for 5 MW and 15 MW wind turbines.

Edgewise instability	Without VGs	With VGs			
		PSO		FO	
Reference wind turbine	Instability angle (°)	Instability angle (°)	Improvement	Instability angle (°)	Improvement
NREL 5 MW	13.87–37.95	20.08–37.95	25.79%	21.02–37.95	29.69%
IEA 15 MW	11.39–32.26	16.18–32.26	22.95%	16.18–32.26	22.95%

behavior is noted when $\Psi > 102°$, where α'_{stall} appears symmetric around $\alpha'_{stall} = 0°$ compared with the situation when $\Psi < 78°$. Thus, optimization within $\Psi < 78°$ can enhance stability even when $\Psi > 102°$. Regarding the range $78° \leq \Psi \leq 102°$, the narrow region of negative ratios suggests a low risk of instability, requiring minimal attention.

This observation implies that the azimuth angle has negligible influence on determining the VG configurations. Consequently,
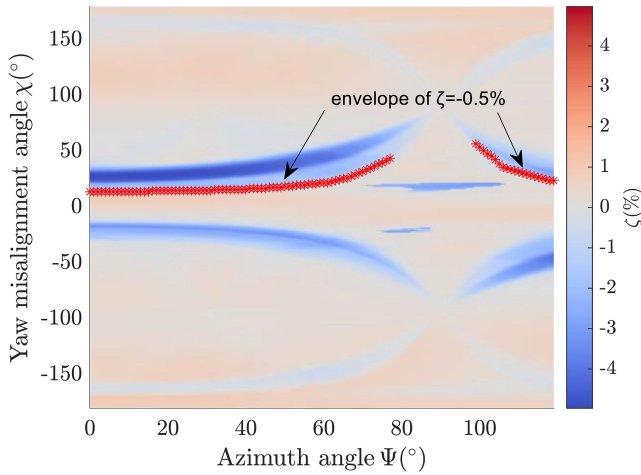
it is recommended to use an azimuth of $\Psi = 0°$ for VG optimization, as discussed above.

5.2 | The Effect of Different Wind Speeds

Section 4 has demonstrated that when placing the VGs at outboard sections, excellent control performance can be observed at a given wind speed. Specifically, at the wind speed of 50 m/s, the

LCO amplitudes of flapwise and edgewise movements decrease obviously, and the LCO range has been narrowed, according to Figure 14. Nevertheless, besides yaw misalignment angle, wind speed has nonnegligible effects on stall-induced instability; thus, the effectiveness of VGs at different wind speeds should also be carefully evaluated to ensure that the optimization is beneficial for all cut-out wind speeds in the aspect of stability performance, or at least not be harmful. Take the NREL 5 MW wind turbine as an example; we select the yaw misalignment angle of 25° and give a wind speed range from 26 to 50 m/s. The VG arrangement is the same as in Section 4.3; the final assessment of LCOs for flapwise and edgewise movements is shown in Figure 20.

From this, we can see that when conducting the optimization at a high wind speed (50 m/s in this study), the VG arrangement is effective for the given wind velocity and beneficial for all wind speeds above the cut-out one. Additionally, focusing on several lower wind speeds, we can conclude that the onset of instability in wind speed is delayed once VGs are installed at the outboard sections of the blade.

5.3 | The Effects for Normal Operating Conditions

Implementing VGs at outboard sections delays the flow separation at the airfoil, increases its lift coefficient, and decreases the drag coefficient. However, we should be cautious in case of negative effects on operational conditions.

We trace the normalized local AoA ($\tilde{\alpha}$) of each airfoil under operating conditions, and the results are shown graphically in Figure 21, where the definition of $\tilde{\alpha}$ is given as
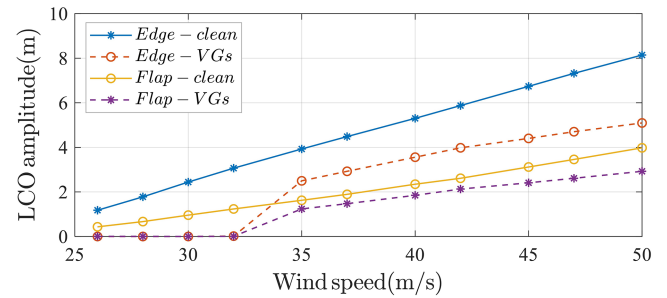
$$\tilde{\alpha} = \frac{\alpha}{\alpha_{stall}} \tag{37}$$

where

$$\alpha = atan\frac{(1-a)V_0}{(1+a')r\Omega} - \theta_t - \beta \tag{38}$$

In which a and a' are axial and tangential inductions, Ω is the spinning angular speed. Furthermore, α_{stall} represents the static stall AoA of each specific airfoil section.

From Figure 21, we can observe that normalized local AoAs for outboard sections (no matter Case 1 or Case 2 in Figure 21) are

FIGURE 18 | The third first-order rotor edgewise damping ratios at different azimuthal and yaw misalignment angles.

FIGURE 20 | LCOs amplitudes of blade tip section at the wind speed $V_0 = 26 - 50$ m/s with the inflow yaw misalignment angle $\chi = 25°$, collective pitch angle $\beta = 90°$.
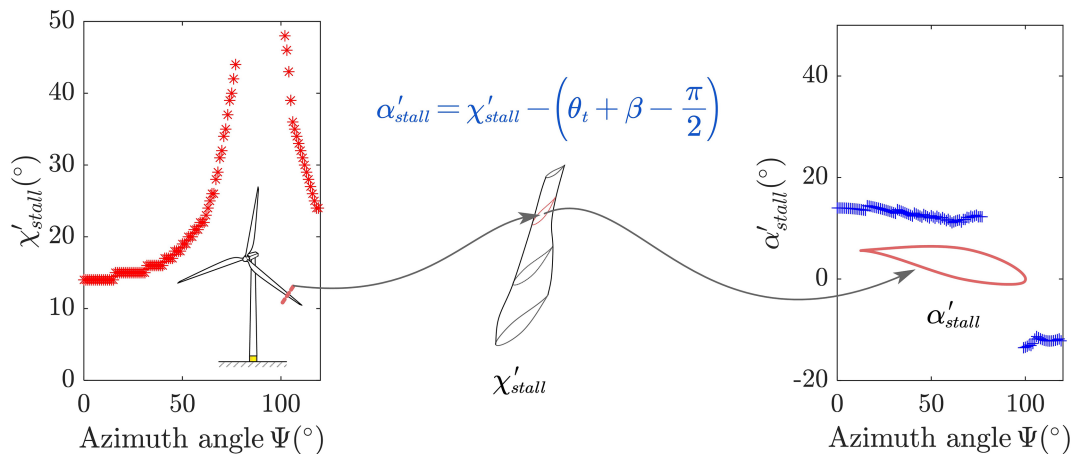
FIGURE 19 | Illustration of transformation between yaw angles χ'_{stall} within rotor level and AoA α'_{stall} within airfoil level.

below 1. This indicates that when a wind turbine is under an operating condition (for situations both below or above the rated wind speed), the local AoAs for VG arrays-corresponded sections are located in Region A in Figure 10. This finding demonstrates that VGs were installed outboard to mitigate the instability without influencing the performance of operating conditions. This is an encouraging result, as the VG array would have little to no negative impact on wind turbines under operating conditions.

This section further explores the integrated outputs, such as wind turbine power and rotor thrust, both with and without VGs installed. The results are illustrated in Figure 22. Notably, the power and thrust performance for VG-equipped wind turbines strongly agree with the clean wind turbines, reinforcing the conclusions drawn from Figure 21. However, some discrepancies

persist, particularly in power and thrust below the rated wind speed, the power and thrust of the VG-equipped FOWT are higher, as VGs enhance the lift coefficient even below the static stall angle, as depicted in Figure 10.

Modern large-scale wind turbines install VGs in the inboard sections to prevent stall in this area, thereby enhancing AEP performance. This study recommends positioning VGs in the outboard sections, ensuring that there is no conflict between the two configurations. Consequently, no interference analysis is required.
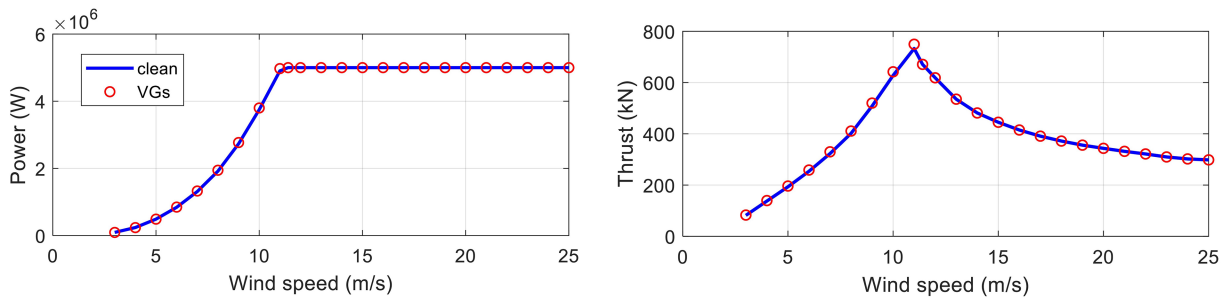
5.4 | The Effects on Tower and Platform

Tower side-side and platform yaw motion responses are depicted in Figure 23, which shows that the presence of VGs effectively mitigates vibrations in the tower's SS direction, as evident from the rapid decay of higher-frequency movements. However, a contrasting trend emerges when examining the platform's yaw mode, which experiences increased severity in vibration. This intriguing observation underscores a fundamental principle: a singular optimization strategy cannot guarantee superior performance across all the critical modes under consideration. To delve further into the mechanics of this phenomenon, it is essential to recognize the distinct roles played by VGs in controlling different modes. Both blade edgewise vibrations and tower side-side motions are primarily influenced by the rate of change of the wind speed to the vertical direction, expressed as $\frac{\partial(\mathrm{d}S)}{\partial V_z}$. On the other hand, the platform's yaw mode is predominantly governed by both $\frac{\partial(\mathrm{d}S)}{\partial V_z}$ and r^2 because the quadratic operation makes the influence from position r prominent. These two parameters can sometimes present conflicting requirements, making optimizing for the best results in all modes simultaneously challenging.

In summary, the analysis presented here underscores the necessity for a multi-objective optimization(MOO) approach when
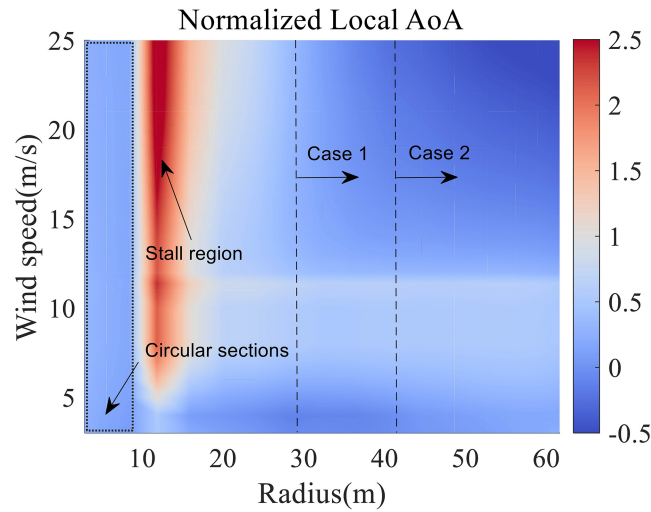
FIGURE 21 | Normalized local AoA at different spanwise positions (radius $r = 1.5 - 63$ m) and wind speed $V_0 = 3 - 25$ m/s under operating conditions.

FIGURE 22 | Power and thrust performance of a normally operating wind turbine with and without VGs equipped.
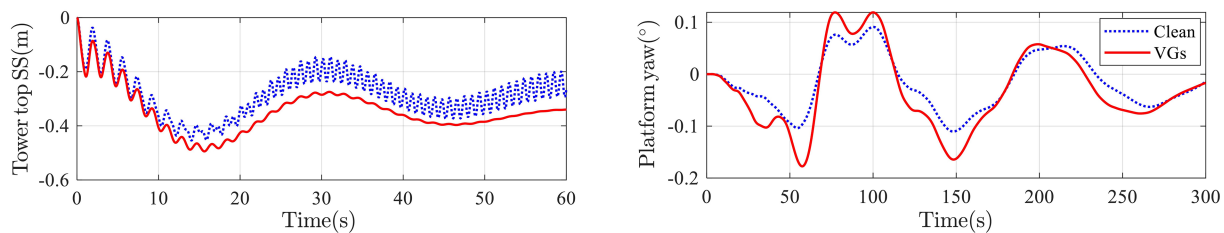
FIGURE 23 | Displacements on tower top and platform DOFs before and after installing VGs, yaw misalignment angle $\chi = 17°$, wind speed $V_0 = 50$ m/s, collective pitch angle $\beta = 90°$.

determining the most effective configuration of VGs. Achieving optimal control over the potentially hazardous modes demands a balance between conflicting factors. Thus, MOO should be conducted in the future.

6 | Conclusion

This paper presented an integrated method for evaluating and mitigating the stall-induced instability of FOWTs under parked conditions with yaw misalignment. The instability evaluation part employed a linear aerodynamic module and a linear hydrodynamics module to analyze the instability behavior of blade, tower, and platform modes. VGs were studied to delay the occurrence of stall-induced instability, and their optimal parameters are achieved by the PSO algorithm in conjunction with the FO method. Numerical results (both linear and nonlinear, frequency domain and time domain) confirm that the installation of VGs arrays does help in mitigating the risk of stall-induced vibration of the edgewise, narrowing the edgewise instability corresponded yaw misalignment angle range by 29.69% and 22.95% for NREL 5 MW and IEA 15 MW wind turbines, respectively. The analysis shows that though the azimuth angle affects aerodynamic damping, it is sufficient only to consider $\Psi = 0°$ in optimizing VG configurations. Implementing VG arrays for outboard sections can increase the onset wind speed of stall-induced instability and have no negative effect on operating conditions. The effects of VGs are also confirmed by nonlinear aerodynamic analysis; nonlinear aerodynamic simulation strengthens the perspective that the VGs help reduce the LCO amplitudes of the blade in their flap-edge plane. This paper also demonstrates that VGs designed specifically for edgewise can lead to better performance of tower SS vibration but slightly worsen on platform yaw motion. In this regard, this paper also recommends performing optimization between different modes using MOO in future work.

In short, this paper proposed including VGs in the outboard section and two optimization strategies to reduce the risk of stall-induced instability, including blade edgewise, tower SS, and platform yaw modes. These strategies have been confirmed through linear and nonlinear analysis, and they are suitable for enhancing stall-induced vibrations in floating wind turbines. However, one limitation of this work depends on the capability of the XFoilVG model to precisely capture the effects of VGs. Finally, the aerodynamic unsteady effects represented by dynamic stall have not been addressed in this study, and more in-depth research is needed in the future to quantify the effects of dynamic loading by considering dynamic stall.

Data Availability Statement

The data that support the findings of this study are available from the corresponding author upon reasonable request.

Peer Review

The peer review history for this article is available at https://www.webofscience.com/api/gateway/wos/peer-review/10.1002/we.70004.

References

1. O. Anaya-Lara, J. O. Tande, K. Uhlen, and K. Merz, *Offshore Wind Energy Technology* (John Wiley & Sons, 2018).

2. J. McMorland, M. Collu, D. McMillan, and J. Carroll, "Operation and Maintenance for Floating Wind Turbines: A Review," *Renewable and Sustainable Energy Reviews* 163 (2022): 112499.

3. P. Veers, C. L. Bottasso, L. Manuel, et al., "Grand Challenges in the Design, Manufacture, and Operation of Future Wind Turbine Systems," *Wind Energy Science* 8, no. 7 (2023): 1071–1131.

4. J. T. Petersen, H. A. Madsen, A. Björck, et al., "Prediction of Dynamic Loads and Induced Vibrations in Stall," 1045. Risø National Laboratory, (1998).

5. C. Chen, J. Zhou, F. Li, and E. Zhai, "Stall-Induced Vibrations Analysis and Mitigation of a Wind Turbine Rotor at Idling State: Theory and Experiment," *Renewable Energy* 187 (2022): 710–727.

6. C. Santhanam, R. Riva, and T. Knudsen, "Surrogate Models for Predicting Stall-Induced Vibrations on Wind Turbine Blades," in *The Science of Making Torque from Wind*, Journal of Physics: Conference Series, Vol. 2265 (IOP Publishing, 2022), 032005.

7. C. Santhanam, R. Riva, and T. Knudsen, "A Study of Stall-Induced Vibrations Using Surrogate-Based Optimization," *Renewable Energy* 214 (2023): 201–215.

8. M. Stettner, M. J. Reijerkerk, A. Lünenschloß, et al., "Stall-Induced Vibrations of the Avatar Rotor Blade," in *The Science of Making Torque from Wind*, Journal of Physics: Conference Series, Vol. 753 (IOP Publishing, 2016), 042019.

9. W. Skrzypiński and M. Gaunaa, "Wind Turbine Blade Vibration at Standstill Conditions the Effect of Imposing Lag on the Aerodynamic Response of an Elastically Mounted Airfoil," *Wind Energy* 18, no. 3 (2015): 515–527.

10. G. Bir and J. Jonkman, "Aeroelastic Instabilities of Large Offshore and Onshore Wind Turbines," in *The Science of Making Torque from Wind*, Journal of Physics: Conference Series, Vol. 75 (IOP Publishing, 2007), 012069.

11. H. Markou, M. H. Hansen, T. Buhl, et al., "Aeroelastic Stability and Control of Large Wind Turbines-Main Results," in *2007 European Wind Energy Conference and Exhibition* (European Wind Energy Association (EWEA), 2007).

12. J. C. Heinz, N. N. Sørensen, V. Riziotis, M. Schwarz, S. Gomez-Iradi, and M. Stettner, "Aerodynamics of Large Rotors. Wp4. Deliverable 4.5," (2016), Report No. 608396.

13. M. H. Hansen, "Improved Modal Dynamics of Wind Turbines to Avoid Stall-Induced Vibrations," *Wind Energy* 6, no. 2 (2003): 179–195.

14. M. H. Hansen, "Aeroelastic Stability Analysis of Wind Turbines Using an Eigenvalue Approach," *Wind Energy* 7, no. 2 (2004): 133–143.

15. P. K. Chaviaropoulos, "Flap/Lead–Lag Aeroelastic Stability of Wind Turbine Blades," *Wind Energy* 4, no. 4 (2001): 183–200.

16. G. Bir, "Multi-Blade Coordinate Transformation and Its Application to Wind Turbine Analysis," in *46th AIAA Aerospace Sciences Meeting and Exhibit* (2008), 1300.

17. R. P. Coleman and A. M. Feingold, "Theory of Self-Excited Mechanical Oscillations of Helicopter Rotors With Hinged Blades," NACA-TR-1351. National Aeronautics and Space Administration, (1957).

18. K. Wang, V. A. Riziotis, and S. G. Voutsinas, "Aeroelastic Stability of Idling Wind Turbines," *Wind Energy Science* 2, no. 2 (2017): 415–437.

19. M. Hansen, *Aerodynamics of Wind Turbines* (Routledge, 2015).

20. K. Thomsen, J. T. Petersen, E. Nim, S. Øye, and B. Petersen, "A Method for Determination of Damping for Edgewise Blade Vibrations," *Wind Energy* 3, no. 4 (2000): 233–246.

21. B. Chen, Z. Zhang, X. Hua, B. Basu, and S. R. K. Nielsen, "Identification of Aerodynamic Damping in Wind Turbines Using Time-Frequency Analysis," *Mechanical Systems and Signal Processing* 91 (2017): 198–214.

22. J. M. Jonkman and B. J. Jonkman, "Fast Modularization Framework for Wind Turbine Simulation: Full-System Linearization," in *The Science of Making Torque from Wind*, Journal of Physics: Conference Series, Vol. 753 (IOP Publishing, 2016), 082010.

23. J. M. Jonkman, A. D. Wright, G. J. Hayman, and A. N. Robertson, "Full-System Linearization for Floating Offshore Wind Turbines in Openfast," in *International Conference on Offshore Mechanics and Arctic Engineering*, Vol. 51975 (American Society of Mechanical Engineers, 2018).

24. M. H. Hansen, L. C. Henriksen, C. Tibaldi, et al., "Hawcstab2 User Manual," (2018).

25. A. Li, Y. Liu, and H. Li, "New Analytical Solutions to Water Wave Radiation by Vertical Truncated Cylinders Through Multi-Term Galerkin Method," *Meccanica* 54 (2019): 429–450.

26. Q. Meng, X. Hua, C. Chen, S. Zhou, F. Liu, and Z. Chen, "Analytical Study on the Aerodynamic and Hydrodynamic Damping of the Platform in an Operating Spar-Type Floating Offshore Wind Turbine," *Renewable Energy* 198 (2022): 772–788.

27. P. K. Chaviaropoulos, E. S. Politis, D. J. Lekou, et al., "Enhancing the Damping of Wind Turbine Rotor Blades, the Dampblade Project," *Wind Energy* 9, no. 1-2 (2006): 163–177.

28. T. Buhl, M. Gaunaa, and C. Bak, "Potential Load Reduction Using Airfoils With Variable Trailing Edge Geometry," *Journal of Solar Energy Engineering* 127, no. 4 (2005): 503–516.

29. W. Li, L. Qiao, G. Li, and Y. Du, "Vibration Control of Large Wind Turbine Blades With Unidirectional Cable Pendulum Damper," *International Journal of Structural Stability and Dynamics* 2022 (2022): 2350082.

30. B. Basu, Z. Zhang, and S. R. K. Nielsen, "Damping of Edgewise Vibration in Wind Turbine Blades by Means of Circular Liquid Dampers," *Wind Energy* 19, no. 2 (2016): 213–226.

31. N. Troldborg, F. Zahle, and N. N. Sørensen, "Simulations of Wind Turbine Rotor With Vortex Generators," in *The Science of Making Torque from Wind*, Journal of Physics: Conference Series, Vol. 753 (IOP Publishing, 2016), 022057.

32. H. Moon, J. Jeong, S. Park, K. Ha, and J.-H. Jeong, "Numerical and Experimental Validation of Vortex Generator Effect on Power Performance Improvement in MW-Class Wind Turbine Blade," *Renewable Energy* 212 (2023): 443–454.

33. D. Baldacchino, "Vortex Generators for Flow Separation Control: Wind Turbine Applications" (Ph.D. Thesis, Delft University of Technology, 2019).

34. Z. Zhao, R. Jiang, J. Feng, et al., "Researches on Vortex Generators Applied to Wind Turbines: A Review," *Ocean Engineering* 253 (2022): 111266.

35. S. Xue, B. Johnson, D. Chao, A. Sareen, and C. Westergaard, "Advanced Aerodynamic Modeling of Vortex Generators for Wind Turbine Applications," in *European Wind Energy Conference (EWEC), Warsaw Poland* (2010).

36. D. A. Griffin, "Investigation of Vortex Generators for Augmentation of Wind Turbine Power Performance," National Renewable Energy Laboratory (NREL), Golden, CO (United States), (1996).

37. H. M. Lee and O. J. Kwon, "Numerical Simulation of Horizontal Axis Wind Turbines With Vortex Generators," *International Journal of Aeronautical and Space Sciences* 20 (2019): 325–334.

38. H. Im, S. Kim, and B. Kim, "Numerical Analysis of the Effect of Vortex Generator on Inboard Region of Wind Turbine Blade," *Journal of Renewable and Sustainable Energy* 13, no. 6 (2021): 063306.

39. W. Würz, B. Plogmann, C. Vetter, and M. Langohr-Kolb, "Wind Tunnel Measurements of the FFA-W3-301 and FFA-W3-360 Airfoils With Vortex Generators and Gurney Flaps," (Universität Stuttgart, Institut Für Aerodynamik und Gasdynamik, 2013).

40. N. N. Sørensen, F. Zahle, C. Bak, and T. Vronsky, "Prediction of the Effect of Vortex Generators on Airfoil Performance," in *The Science of Making Torque from Wind*, Journal of physics: conference series, Vol. 524 (IOP Publishing, 2014), 012019.

41. D. De Tavernier, D. Baldacchino, and C. Ferreira, "An Integral Boundary Layer Engineering Model for Vortex Generators Implemented in Xfoil," *Wind Energy* 21, no. 10 (2018): 906–921.

42. J. Jonkman, S. Butterfield, W. Musial, and G. Scott, "Definition of a 5-MW Reference Wind Turbine for Offshore System Development," NREL/TP-500-38060. National Renewable Energy Laboratory (NREL), Golden, CO (United States), (2009).

43. J. Jonkman, "Definition of the Floating System for Phase IV of OC3," NREL/TP-500-47535. National Renewable Energy Lab (NREL), Golden, CO (United States), (2010).

44. E. Gaertner, "Definition of the IEA 15-Megawatt Offshore Reference Wind," NREL/TP-5000-75698. National Renewable Energy Lab (NREL), Golden, CO (United States), (2020).

45. Q. Meng, W. Yu, F. Wu, X. Hua, and C. Chen, "Stall-Induced Aeroelastic Instability of Floating Offshore Wind Turbines: Comparison of Time Domain and Frequency Domain Quasi-Steady Approaches," (2025), Under Review.

46. J. M. Jonkman, "Dynamics of Offshore Floating Wind Turbines-Model Development and Verification," *Wind Energy: An International Journal for Progress and Applications in Wind Power Conversion Technology* 12, no. 5 (2009): 459–492.

47. B. W. McCormick, *Aerodynamics, Aeronautics, and Flight Mechanics* (John Wiley & Sons, 1994).

48. J. M. Jonkman, "Dynamics Modeling and Loads Analysis of an Offshore Floating Wind Turbine" (Ph.D. Thesis, University of Colorado, Boulder, 2007).

49. L. Chen, B. Basu, and S. R. K. Nielsen, "A Coupled Finite Difference Mooring Dynamics Model for Floating Offshore Wind Turbine Analysis," *Ocean Engineering* 162 (2018): 304–315.

50. R. R. Craig Jr and A. J. Kurdila, *Fundamentals of Structural Dynamics* (John Wiley & Sons, 2006).

51. H. Grandis and Y. Maulana, "Particle Swarm Optimization (PSO) for Magnetotelluric (MT) 1D Inversion modeling," in *Southeast Asian Conference on Geophysics*, IOP conference series: Earth and Environmental Science, Vol. 62 (IOP Publishing, 2017), 012033.

52. A. G. Gad, "Particle Swarm Optimization Algorithm and Its Applications: A Systematic Review," *Archives of Computational Methods in Engineering* 29, no. 5 (2022): 2531–2561.

53. J. Lohmann, "Non-Linear Stall-Induced Instability Analysis of a Parked Rotor" (Master's Thesis, Delft, The Netherlands, 2024).

54. W. Yu, L. K. Bajarūnas, A. Zanon, and C. arlosJ. S. Ferreira, "Modeling Dynamic Stall of an Airfoil With Vortex Generators Using a Double-Wake Panel Model With Viscous–Inviscid Interaction," *Wind Energy* 27, no. 3 (2024): 277–297.

55. L. A. Viterna and R. D. Corrigan, "Fixed Pitch Rotor Performance of Large Horizontal Axis Wind Turbines," in *Large Horizontal-Axis Wind Turbines* (NASA Lewis Research Center, 1982).

Appendix A: Expressions for Partial Derivatives

Expressions for several partial derivatives are given as

$$
\begin{aligned}
\frac{\partial(\mathrm{d}T)}{\partial V_y} &= \frac{1}{2}\frac{\rho c}{V'_0}\left[V_y V_z C_l + \left(2V_y^2 + V_z^2\right)C_d + V_z^2\frac{\partial C_l}{\partial\alpha} + V_y V_z\frac{\partial C_d}{\partial\alpha}\right] \\
\frac{\partial(\mathrm{d}T)}{\partial V_z} &= \frac{1}{2}\frac{\rho c}{V'_0}\left[\left(2V_z^2 + V_y^2\right)C_l + V_y V_z C_d - V_y V_z\frac{\partial C_l}{\partial\alpha} - V_y^2\frac{\partial C_d}{\partial\alpha}\right] \\
\frac{\partial(\mathrm{d}S)}{\partial V_y} &= \frac{1}{2}\frac{\rho c}{V'_0}\left[-\left(2V_y^2 + V_z^2\right)C_l + V_y V_z C_d - V_y V_z\frac{\partial C_l}{\partial\alpha} + V_z^2\frac{\partial C_d}{\partial\alpha}\right] \\
\frac{\partial(\mathrm{d}S)}{\partial V_z} &= \frac{1}{2}\frac{\rho c}{V'_0}\left[-V_y V_z C_l + \left(V_y^2 + 2V_z^2\right)C_d + V_y^2\frac{\partial C_l}{\partial\alpha} - V_y V_z\frac{\partial C_d}{\partial\alpha}\right]
\end{aligned}
\tag{A1}
$$